



**COMPUTATIONAL MODEL OF ONE-DIMENSIONAL
DIELECTRIC BARRIER DISCHARGES**

THESIS

Krista G. Marchand , Captain, USAF
AFIT/GAP/ENP/05-05

**DEPARTMENT OF THE AIR FORCE
AIR UNIVERSITY
AIR FORCE INSTITUTE OF TECHNOLOGY**

Wright-Patterson Air Force Base, Ohio

APPROVED FOR PUBLIC RELEASE; DISTRIBUTION UNLIMITED

The views expressed in this thesis are those of the author and do not reflect the official policy or position of the United States Air Force, Department of Defense, or the United States Government.

AFIT/GAP/ENP/05-05

COMPUTATIONAL MODEL OF ONE-DIMENSIONAL
DIELECTRIC BARRIER DISCHARGES

THESIS

Presented to the Faculty

Department of Engineering Physics

Graduate School of Engineering and Management

Air Force Institute of Technology

Air University

Air Education and Training Command

in Partial Fulfillment of the Requirements for the

Degree of Master of Science (Applied Physics)

Krista G. Marchand , BS
Captain, USAF

June 2005

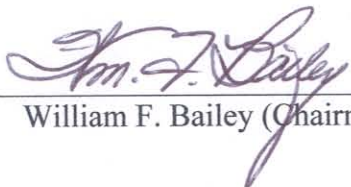
APPROVED FOR PUBLIC RELEASE; DISTRIBUTION UNLIMITED

AFIT/ENP/GAP/05-05

COMPUTATIONAL MODEL OF ONE-DIMENSIONAL
DIELECTRIC BARRIER DISCHARGES

Krista G. Marchand , BS
Captain, USAF

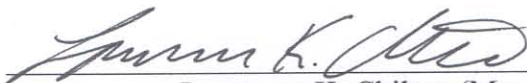
Approved:



William F. Bailey (Chairman)

3 June '05

date



Lawrence K. Chilton (Member)

3 Jun 05

date



Christopher G. Smithtro (Member)

3 Jun 05

date

Abstract

As theory lags experiment for dielectric barrier discharge flow control, two different computational methods are implemented to give further insight into characteristics of the dielectric barrier discharge (DBD). A one-dimensional fluid model of a surface-type dielectric barrier discharge is created using He as the background gas. This simple model, which only considers ionizing collisions and recombination in the electropositive gas, creates an important framework for future studies into the origin of experimentally observed flow-control effects of the DBD. The two methods employed in this study include the semi-implicit sequential algorithm and the fully implicit simultaneous algorithm. The first involves consecutive solutions to Poisson's, the electron continuity, ion continuity and electron energy equations. This method combines a successive over-relaxation algorithm as a Poisson solver with the Thomas algorithm tridiagonal routine to solve each of the continuity equations. The second algorithm solves an $Ax=b$ system of linearized equations simultaneously and implicitly. The coefficient matrix for the simultaneous method is constructed using a Crank-Nicholson scheme for additional stability combined with the Newton-Raphson approach to address the non-linearity and to solve the system of equations. Various boundary conditions, flux representations and voltage schemes are modeled. Test cases include modeling a transient sheath, ambipolar decay and a radio-frequency discharge. Results are compared to validated computational solutions and/or analytic results when obtainable. Finally, the semi-implicit method is used to model a DBD streamer.

Acknowledgments

Always first, to my amazing husband who has the most wonderful gypsy soul I have ever encountered --- I thank him for all the joy and beauty that he helps me see. I could never have completed this degree without his support and encouragement.

Next, I thank my determined and caring classmates who ensured that I passed my classes even during the most difficult quarters. Their surrogate strength and intellectual assist made the world of difference. Along these same lines, I have to thank an entire entourage of friends who have called, listened and cared: Junebug, Gretchen, Angie, Ken, Sally, Silinda, Bethany.

Last but certainly not least, I thank my advisor and each of my committee members. My advisor, Dr. Bailey, knows more about every subject of physics than I ever thought possible. His wisdom and encouragement have made all the difference for my completion of this degree. I also thank Dr. Chilton and Maj Smithtro for their time and wonderful advice.

As a special note for my father – I certainly could not have done this without your support over all these years. The math games that we played on our family trips to the lake and swim meets will always be one of the fondest memories I carry with me. I have always respected both your mathematical gift and your strength of character. I hope that I make you as proud of me as I am of you.

Krista Grace Marchand

Table of Contents

	Page
Abstract	iv
Acknowledgments	v
List of Figures	viii
List of Tables	x
 I. DBD History and Applications	 1
Brief History	2
AF Applications	2
Plasma Dynamics	3
Dielectric Barrier Discharge	5
Recent Experimental Work	6
Numerical Efforts	9
 II. Fluid Approach to DBD Simulation	 11
The Boltzmann Equation	11
The Fluid Equations	12
Transport Coefficients	14
Sources and Sinks	19
Poisson's Equation	24
 III. DBD Computational Development	 27
Spatial Discretization	27
Scharfetter-Gummel Flux Discretization	29
Boundary Conditions	33
The Dielectric Boundary	35
1-D Numerical Methods	38
Semi-implicit Sequential	38
SOR	41
Tridiagonal	43
Semi-Implicit Summary	46
Fully Implicit Simultaneous	46
Crank-Nicholson	47
Newton-Raphson	48
Fully Implicit Summary	53

IV.	Computational Validation and DBD Results.....	55
	Validation.....	55
	Analytic Poisson	56
	Transient Sheath.....	59
	Ambipolar Decay	62
	Radio-Frequency Glow Discharge.....	70
	The DBD Streamer	76
V.	DBD Modeling – Accomplishments and the Next Round.....	82
	Looking Back.....	82
	Accurate 1-D Model	82
	Fully Implicit Advantages.....	83
	DBD Streamer Characterization	84
	Looking Forward	84
	Fully Implicit Development.....	84
	Mean Velocity Flux	85
	Continued Dielectric Studies	85
	Appendix A. Model Assumptions.....	87
	Appendix B. Newton-Raphson Matrix	88
	Appendix C. Transport/Rate Coefficients Fit	94
	Bibliography	96

List of Figures

Figure	Page
1. Basic Plasma Discharge Configuration	3
2. Current/Voltage Discharge Classification (11:84).....	4
3. Equivalent Circuit Model of DBD	5
4. Actuator-On Lift Increase (1:3)	7
5. Actuator Reattachment of Flow (2:8)	7
6. Induced Airflow in Initially Still Air (3:2125)	8
7. Asymmetric Electrode	8
8. Electron Mobility Coefficient in Helium at 1 Torr (17)	16
9. Ion Mobility Coefficient in Helium at 1 Torr (18)	16
10. Electron Diffusion Coefficient in Helium at 1 Torr (17).....	18
11. Ionization Frequency in Helium (17).....	21
12. Electron Energy Loss Frequency in Helium (17)	23
13. Grid format.....	28
14. Grid Designation - ‘i’ Index.....	28
15. $F1[Z]$ and $F2[Z]$	30
16. 1-D Dielectric Configuration	36
17. Dielectric Grid Geometry	37
18. Semi-Implicit Sequential Iterative Scheme	40
19. Poisson Check – No Dielectric	58
20. Poisson Check – Dielectric Inserted	58
21. Transient Sheath – Sheath Progression.....	61

22. Transient Sheath – Electric Potential Progression	61
23. Ambipolar Diffusion (4:28)	62
24. Ambipolar Particle Densities – Analytic and Computational	66
25. Ambipolar Electric Field – Analytic and Computational	66
26. Natural Log of Peak Density – Ambipolar Decay	67
27. Time-Dependent Peak Densities	69
28. Percent Error for Peak Density Decay	70
29. Semi-Implicit RF Densities and Electric Fields	72
30. Results from Hilbun – RF Densities and Electric Fields (16:12)	72
31. RF Current Densities at Left Electrode	74
32. Results from Hilbun – RF Current Densities (16:13)	75
33. Dielectric Circuit Configuration for Streamer Simulation	77
34. DBD Streamer Evolution	79

List of Tables

Table	Page
1. Node and Half Node Values	27

COMPUTATIONAL MODEL OF ONE-DIMENSIONAL DIELECTRIC BARRIER DISCHARGES

For this project, the interest in the dielectric barrier discharge (DBD) stems from its application to the plasma actuator. The plasma actuator is a flow control device with no moving parts, does not change airfoil shape and puts no parts in the flow. Many experimental endeavors are already underway studying the capabilities of the plasma actuator (1;2;3). Observation without physical explanation leaves much to be desired. The computational side of this technology has yet to fully describe the plasma actuator phenomena theoretically. This project tests and validates a numerical model that is ultimately used to simulate a one-dimensional DBD in order to study the effect of the dielectric barrier on the discharge.

I. DBD History and Applications

The DBD has an extensive background in both industrial and scientific applications. While the basic theory of the DBD can be found in most plasma dynamics texts (4; 5), flow control DBD devices extend operations beyond the domain of current theory. The scientific community is currently attempting to remedy this shortcoming. This chapter gives a brief history of the DBD, introduces the basic theory and reviews recent experimental and computational endeavors.

Brief History

Much of the research on “silent discharges” – another name for the DBD – finds its roots in the evolution of industrial processes. The original experimental set-up driving the DBD can be traced to 1857 when Siemens proposed a special electrical discharge to produce ozone (6:309). In 1955, Tanaka discovered that the DBD could be used for excimer formation in rare gases (6:309). By 1960, Bitzer and Slottow applied this discovery to the invention of the plasma display panel (PDP) (7:R54). First developed as a monochrome display for educational purposes, the PDP has nearly superseded the cathode ray tube for retail color television technology. While current DBD investigations include a wide variety of applications, one of significant interest to the Air Force is DBD flow control.

AF Applications

With contemporary Air Force weapons systems progressing toward smaller, faster, smarter designs, any scientific endeavor that could possibly further that evolution is on the forefront of the military scope. Compared with the now-archaic BLU-109 bomb, the smart bomb offers identical penetration capabilities in a package one-third the diameter, half the length and only an eighth of the total weight (8:7). As things get smaller, they get faster and smarter simultaneously. Current operations require GPS equipped small-diameter bombs with top-of-the-line control systems ranging from lattice folding fins to laser guidance (8:7). These recent developments have given US military forces the ability to do things never dreamed of in the past.

As more and more warfighters express an interest in continuing to enhance the agility of their weapons, technology simultaneously approaches its miniaturization limit for control systems. A new flow control device would greatly enhance the ability to continue decreasing the size and increasing the control capabilities of future combat technologies. The DBD plasma actuator could possibly be a part of this future. While actuator flow control is a very advanced subject, the physical laws driving the device originate in the basic physics of plasma dynamics.

Plasma Dynamics

In general, a gas discharge is generated by power input to a background gas maintained in a capacitive set-up between two electrodes (Fig.1). The voltage source can be either AC or DC. For each source, the potential difference (or alternating potential difference) between the electrodes establishes an electric field. The field accelerates electrons – either free in the gas or pulled from the cathode – through the background gas. Some of these translational electrons collide with the neutral particles in the background gas generating ion/electron pairs.



Figure 1. Basic Plasma Discharge Configuration

At a certain value of applied potential, the electrons gain enough energy to create an electron avalanche. One seed electron accelerates through the field to a high enough

energy to knock an additional electron off neutral particles or other positive/negative ions. These additional electrons accelerate and cause even more ionization. This process is known as breakdown and the potential difference required to initiate it is the breakdown voltage.

A self-sustaining discharge occurs when the applied voltage is large enough to initiate breakdown. In any type of self-sustaining discharge, the cathode sheath plays an integral role because most of the ionization sustaining the discharge occurs in this region. The size of the sheath is very small and depends on the type and pressure of the background gas (9:134). The cathode sheath of a DC discharge has net positive charge that essentially shields the rest of the discharge from the cathode potential (10:9). The effective potential difference for the non-sheath plasma is greatly diminished because of the significant potential drop that occurs in the sheath.

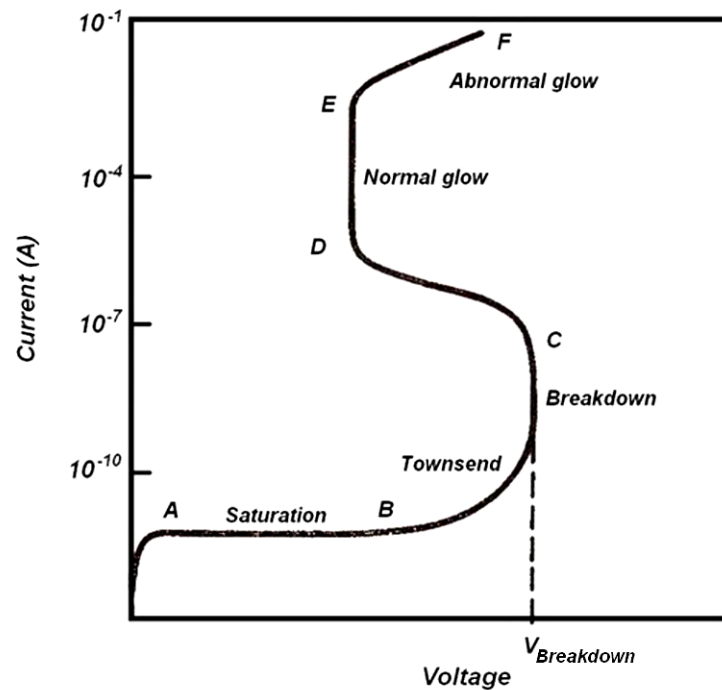


Figure 2. Current/Voltage Discharge Classification (11:84)

Once breakdown has occurred and the sheath has been established, gas discharges are classified according to characteristic voltage, current and pressure ranges as shown in Fig. 2. Since the DBD is a special case of the glow discharge, this region of the chart of discharge classification is of most interest to this project. The gas in a glow discharge is only weakly ionized (10:9) but the ionization has not dropped low enough to lose its plasma characteristics. The common qualities of low pressures ($\sim 1\text{-}10$ Torr), low currents ($\sim 10^{-6} - 10^{-1}$ A) and high voltages ($\sim 10^2 - 10^3$ V) generally distinguish this type of discharge (9:2-4).

Dielectric Barrier Discharge

The DBD finds its home near the high-end of the glow discharge pressure spectrum. As the name suggests, a dielectric barrier is inserted into the discharge system by coating one or both of the electrodes. This barrier blocks all (or most) of the current flow to the buried electrode and alters the electric potential across the discharge.

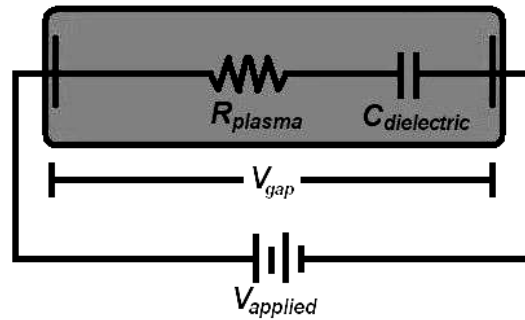


Figure 3. Equivalent Circuit Model of DBD

Effectively, the dielectric barrier creates a capacitance in the discharge circuit. As an example in Fig. 3, if a large negative potential is applied to the left electrode then

electrons will accelerate toward the right electrode. If this electrode is covered with a dielectric that blocks current and accumulates this charge, this scenario is analogous to charging a capacitor in a DC circuit. The electron current, had the barrier not been inserted, turns into displacement current. Assuming that the plasma has some characteristic resistance, the discharge becomes a capacitive circuit (Fig. 3).

The charge build-up on the dielectric surface dramatically changes the discharge behavior. When the applied voltage is DC, the charge accumulation eventually reduces the effective electric field eventually driving the field to zero and extinguishing the discharge all-together. In an AC discharge, the charge accumulation on the dielectric surface may give a large number of seed electrons for the backward stroke (as opposed to the assumed few seed electrons on the forward stroke). Some numerical models predict that this asymmetry is the source of the experimentally observed flow control (12:9; 13:11).

Recent Experimental Work

Experimental research has proven that the DBD can be used as a flow control device. In wind tunnels, an actuator-equipped airfoil has been shown to attain higher angles of attack before separation and stall occur (1:3). This coincides with the increased coefficient of lift associated with having the actuator turned on (Fig.4). In this experiment, a higher coefficient of drag was simultaneously observed when only one actuator was used. However, when four actuators were placed in series along the camber, the increased coefficient of lift was maintained while the increased drag was essentially eliminated.

Experiment has also documented that the actuator can reattach separated flow (2:8). Fig. 5 shows the flow visualization created by introduction of smoke streaklines into the flow. The top picture shows the separated, turbulent flow under the airfoil and the bottom picture shows reattached, laminar flow. The only configuration change between the two photos is the actuator power.

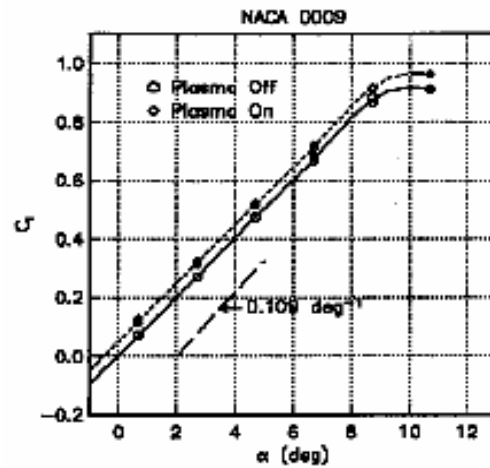


Figure 4. Actuator-On Lift Increase (1:3)

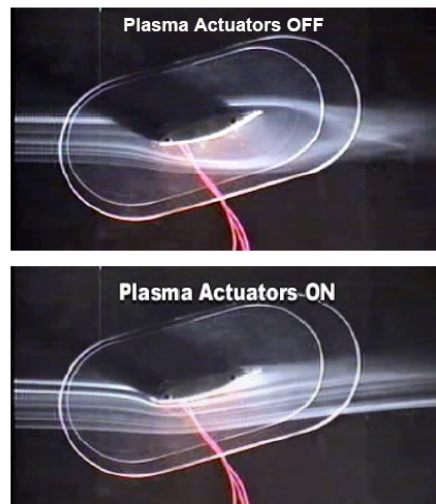


Figure 5. Actuator Reattachment of Flow (2:8)

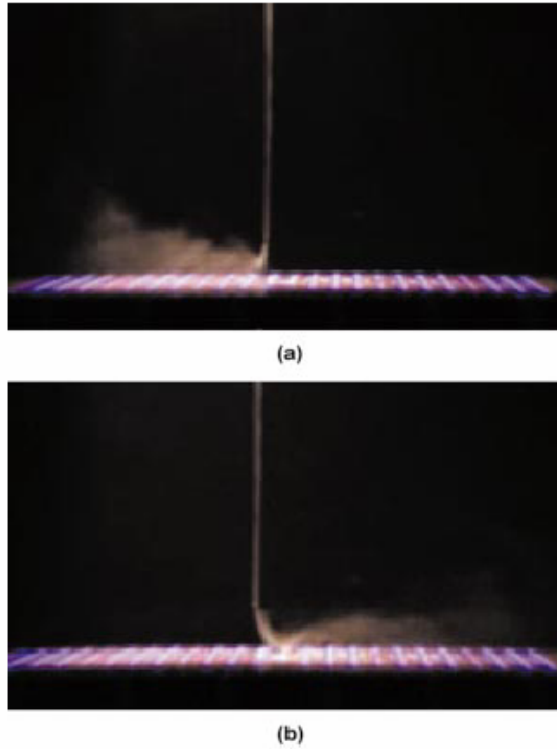


Figure 6. Induced Airflow in Initially Still Air (3:2125)

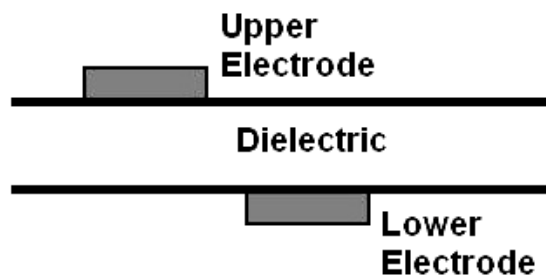


Figure 7. Asymmetric Electrode

Finally, the actuator has been shown to induce flow in initially still air. Fig. 6 shows titanium dioxide smoke emitted from a vertical tube 2.5mm above a series of asymmetric electrodes (3:2125). Each asymmetric electrode consists of one exposed electrode sitting on top of the dielectric and one electrode sitting immediately adjacent on

the bottom surface of the dielectric as shown in Fig. 7. Each asymmetric electrode induces neutral gas flow. With the electrodes phased so that they can accelerate the air flow, the smoke moves to the right or left according to the phasing of the electrodes. The only configuration change between the two pictures in Fig. 6 is the phasing.

Experimental results definitively show that the DBD plasma actuator influences or creates airflow. In order to maximize actuator capabilities, however, scientists must be able to theoretically explain the results. Numerous computational groups are working to discover the source and nature of airflow alteration when the DBD actuator is engaged.

Numerical Efforts

Creating a numerical model of DBD flow control is a difficult endeavor. Keeping track of huge particle densities ($\sim 10^{15} - 10^{20}$ particles/cm³), differing species, a variety of possible particle relations (momentum transfer, excitations, ionization, electrical interactions) and varying electric field configurations proves to be a significant challenge. In the past twenty years with the advent of continually improving computers and processors, many numerical models have made their way into academic periodicals each building on and/or fine-tuning some previous set of calculations.

While there are far too many models to cover each in depth, this project primarily utilizes the work of Boeuf and Pitchford, Hilbun and Font (14; 15; 16; 12) as guides for the numerical model and validation tests. Two Boltzmann solvers, BOLSIG and SIGLO-RF (17; 18), are used to generate the rates/transport coefficients as well as results for qualitative comparison. BOLSIG determines the solution to the Boltzmann equation for electrons in weakly ionized gases. These solutions assume steady-state, uniform fields

and can be calculated for fifteen different gases and a wide range of reduced field values (19:1). SIGLO-RF is a one-dimensional fluid model of a radio-frequency, low pressure discharge. This code gives the ion density, electron density and electric field as functions of time and one-dimensional space (20:1). Once again, fifteen different gases can be modeled.

So far, computational projects have only calculated a relatively small asymmetry associated with the DBD. Font reports a time averaged computational force of 1.5×10^{-3} N (12:9) for an actuator 250mm wide. This force is roughly equivalent to the weight of $1/40^{\text{th}}$ of a teaspoon of salt. The importance of the DBD model greatly increases knowing that the search could be likened to measuring the effect of several grains of salt on the wind. Using basic fluid dynamic principles to model an actuator in one-dimension, exploring both AC and DC field sources and the addition of a dielectric substrate, this project will help further establish the dielectric barrier effect on discharge current. This paper covers the basic theory and equations, computational development, numerical validation and results for the DBD streamer simulation.

II. Fluid Approach to DBD Simulation

While there are several methods that could be employed to model the DBD, this project utilizes the fluid approach. The fluid approach assumes that microscopic detail is unnecessary for determining macroscopic behavior. The background theory and model development are covered in this chapter. Unless otherwise specified, all variables and equations are expressed in terms of SI units.

The Boltzmann Equation

Like many problems relating to plasmas, this story begins with the Boltzmann equation

$$\frac{\partial f_s}{\partial t} + \vec{v} \cdot \vec{\nabla} f_s + \vec{a} \cdot \vec{\nabla}_{\vec{v}} f_s = \left(\frac{\partial f_s}{\partial t} \right)_{collision} . \quad (1)$$

The solution to this equation, $f_s(x, y, z, v_x, v_y, v_z, t)$, gives the time-dependent single particle distribution function in phase space (21:11). A particle in Eq. (1) is of type “s,” has velocity \vec{v} and acceleration \vec{a} . The subscript “s” could designate electrons, positive ions, negative ions or neutrals. The first gradient, $\vec{\nabla} f_s$, represents the change to the distribution function with respect to configuration coordinates, (x, y, z) , whereas the second gradient, $\vec{\nabla}_{\vec{v}} f_s$, represents the change to the distribution function with respect to the velocity coordinates, (v_x, v_y, v_z) . The right-hand side accounts for the changes to the distribution function brought about by collisions (21:12).

The solution to the Boltzmann equation represents the number of particles in a volume element $dx \cdot dy \cdot dz$ at position $x = (x, y, z)$ and the velocity volume element $dv_x \cdot dv_y \cdot dv_z$ with velocity $\vec{v} = (v_x, v_y, v_z)$ at time t (22:30). This solution gives a detailed, microscopic view of any given plasma system at any given time. Many times, due to the complexity of associated systems, it is impossible to find an analytic solution and/or unwieldy to calculate for every time step in the process. When the system under investigation does not require microscopic detail, the fluid equations provide a more practical alternative for solution.

The Fluid Equations

The fluid equations are derived by taking velocity moments of the Boltzmann equation. The n th velocity moment can be represented as (21:19):

$$\int \vec{v}^n \left[\frac{\partial f_s}{\partial t} + \vec{v} \cdot \vec{\nabla} f_s + \vec{a} \cdot \vec{\nabla}_{\vec{v}} f_s = \left(\frac{\partial f_s}{\partial t} \right)_{collision} \right] dv_x dv_y dv_z . \quad (2)$$

These moments generate equations in terms of macroscopic variables that can be measured or, in the case of this study, solved for computationally. The details of their derivation will not be covered here but can be found in elementary plasma references (21:19-26; 22:39-42).

The model assumptions become important to the simplification of each of the moments. The model assumptions for this project along with their associated simplifications are discussed in Appendix A. The simplified zeroth moment yields the particle continuity equation:

$$\frac{\partial n_s}{\partial t} + \bar{\nabla} \cdot (n_s \bar{v}_s) = S_s \quad (3)$$

where n_s is the density of the particle of type “s,” \bar{v}_s is average particle velocity and S_s is the particle source/loss function (22:39). The first moment gives the particle momentum equation, which can be simplified to yield the drift-diffusion flux approximation:

$$\bar{\Gamma}_s = n_s \bar{v}_s = \mp n_s \mu_s \bar{E} - D_s \bar{\nabla} n_s \quad (4)$$

where $\bar{\Gamma}_s$ represents the flux of “s” type particles, \bar{E} is the electric field, $\mp \mu_s$ is the mobility coefficient and D_s is the free diffusion coefficient of particle of type “s” (14:1378). The selected sign of the mobility term matches that of the charge of the particle. Finally, the second moment is the electron energy equation which in simplified form greatly resembles Eq. (3):

$$\frac{\partial (n_e u_e)}{\partial t} + \frac{5}{3} \bar{\nabla} \cdot \bar{\Gamma}_e = S_e \quad (5)$$

where u_e represents the average electron energy, S_e represents the electron energy source/loss function (10:4). The electron energy density flux is given by

$$\bar{\Gamma}_e = -(n_e u_e) \mu_e \bar{E} - D_e \bar{\nabla} (n_e u_e). \quad (6)$$

The continuity and momentum equations are considered sufficient to model ion transport because the local field approximation is applied (10:14). This approximation

assumes a direct relationship between the particle energy distribution and the electric field. For the electrons, however, this approximation is questionable. Therefore, the electron energy can not be directly related to the local field and Eq. (5) must be solved in addition to Eqs. (3) and (4) in order to more accurately characterize electron behavior.

The computational variables for this project are n_e , $\bar{\Gamma}_e$, n_p , $\bar{\Gamma}_p$, $(n_e u_e)$, $\bar{\Gamma}_e$ and \bar{E} . While Eqs. (3)-(6) give us the ability to solve for the first six of these variables, the transport parameters, source/loss terms and vital sixth variable remain undetermined. Evaluation of the electric field requires a self-consistent solution of Poisson's equation and will be covered in the next section. The transport coefficients (μ_s and D_s) and the production/loss rates, essential to an accurate form of the fluid equations, will be covered immediately. Note that for this study, the values for all transport coefficients and source/loss rates are evaluated by a numerical solution of the collisional Boltzmann equation (17; 18).

Transport Coefficients

Transport coefficients specify the macroscopic properties of the plasma and are determined from a selected weighting of the distribution function. These coefficients are typically expressed as functions of average energy or the reduced electric field expressed as E/N or E/p (9:17). The reduced field in terms of the number density (E/N) has units of *Townsend* (Td) where

$$1 \cdot Td = 1 \times 10^{-17} V \cdot cm^2. \quad (7)$$

Ignoring local pressure variations, E/N is related to E/p by the ideal gas law

$$p = Nk_b T \quad (8)$$

where p is the pressure of the gas, N is the neutral number density, k_b is Boltzmann's constant and T is the temperature of the gas. Assuming the temperature is $300^\circ K$ then

$$3 \cdot Td \approx 1 \cdot V / cm / torr . \quad (9)$$

The transport coefficients each apply to one term of the drift-diffusion flux approximation:

$$\bar{\Gamma}_s = \underbrace{\mp n_s \mu_s \bar{E}}_1 - \underbrace{D_s \bar{\nabla} n_s}_2 . \quad (10)$$

In the first term of Eq. (10), the mobility coefficient μ_s relates the proportionality between the drift velocity of a charged particle and the field:

$$\bar{v}_{d,e} = -\mu_e [u_e] \bar{E} \quad (11)$$

and

$$\bar{v}_{d,p} = \mu_p [E / p] \bar{E} \quad (12)$$

where $\bar{v}_{d,e}$ is the drift velocity of the electron (9:11), $\bar{v}_{d,p}$ is the drift velocity of the ion, $\mu_e [u_e]$ is the electron mobility based on the local average electron energy, E / p is the local reduced field expressed in terms of pressure and $\mu_p [E / p]$ is the ion mobility based on the local reduced field.

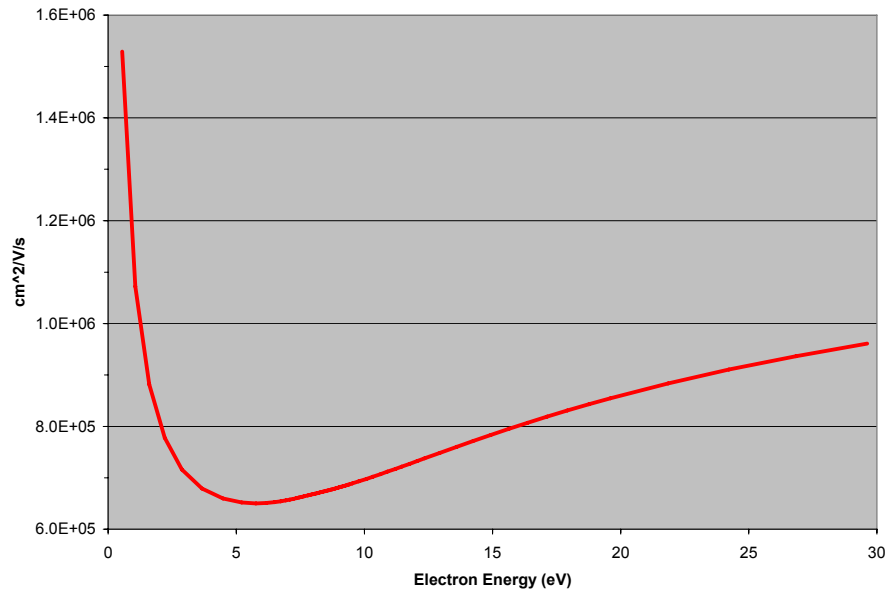


Figure 8. Electron Mobility Coefficient in Helium at 1 Torr (17)

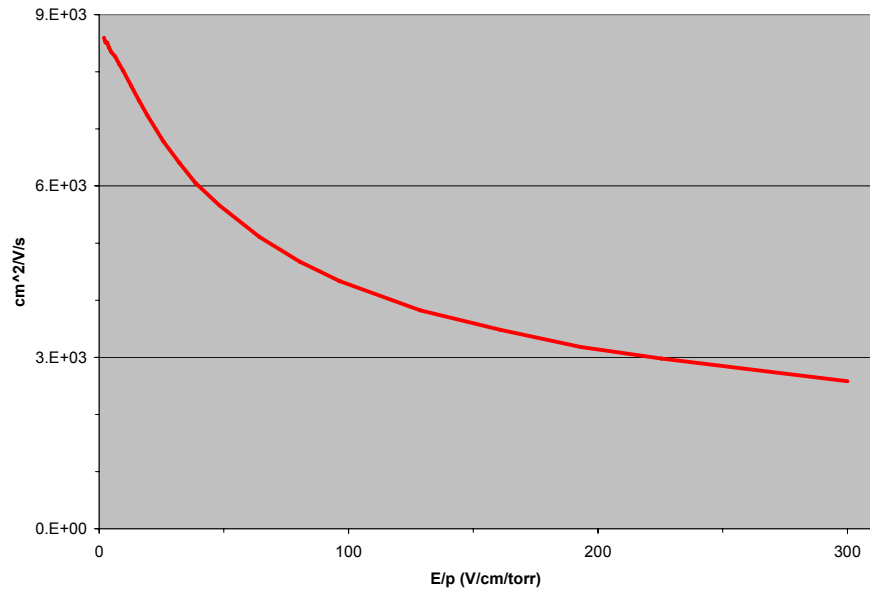


Figure 9. Ion Mobility Coefficient in Helium at 1 Torr (18)

The difference between the ion and electron mobility functional dependence is once again based on the local field approximation. Because the ion energy distribution

can be directly related to the local field, the ion mobility is considered to be a function of the reduced field. The electron mobility is a function of the average electron energy because the local field approximation does not apply.

Figs. 8 and 9 give examples of the ion and electron mobility in helium gas. The plot domains are limited to the energy and reduced field values that are most commonly encountered in a helium discharge. Also note from Figs. 8 and 9 that the electron mobility is two to three orders of magnitude greater than the ion mobility.

The magnitude of the electron mobility contributes significantly to the stiffness of the electron equations because the response of the electron velocity to the field can change a great deal over a small spatial range. The reduced magnitude of the ion mobility means that the ions are not nearly as responsive to the field. Because of this, many numerical models use either a constant ion mobility or an equation that characterizes the ion mobility for certain large ranges of the reduced field (15:5611; 23:2789).

The transport coefficient associated with part 2 of Eq. (10) is the diffusion coefficient D . The diffusion coefficient is determined by

$$D = \left\langle \frac{\bar{v}^2}{3\nu_m} \right\rangle \quad (13)$$

where \bar{v} is the velocity of the particle and ν_m is the effective collision frequency for momentum transfer (5:9; 20). This parameter quantifies the flux associated with the spatial non-uniformity of the particle or energy density in the gas. The electron diffusion coefficient in helium is shown in Fig. 10.

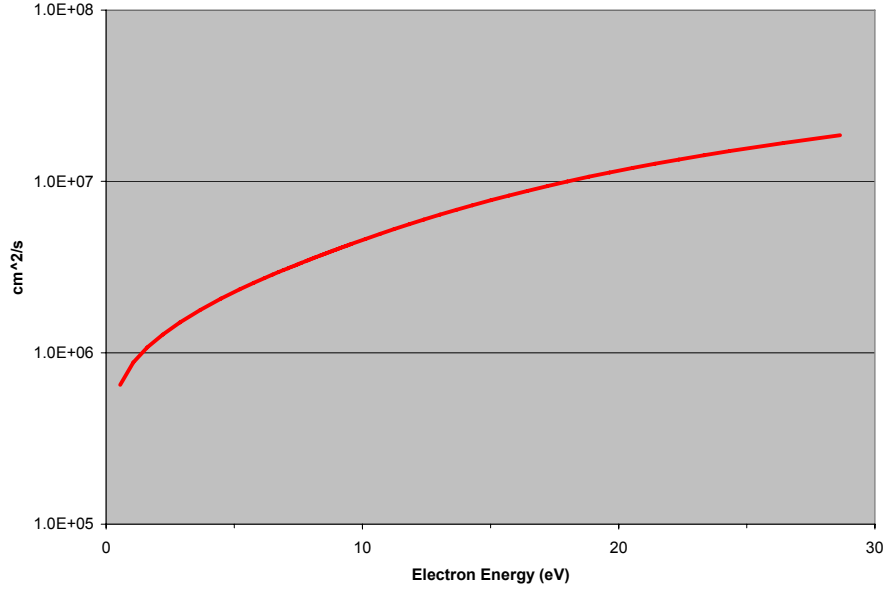


Figure 10. Electron Diffusion Coefficient in Helium at 1 Torr (17)

The diffusion coefficient for electrons is assumed to be a function of the average energy determined by the energy continuity equation. The ion diffusion coefficient is a function of E/p and directly related to the ion mobility coefficient. Since the ions are assumed to have a Maxwellian distribution, the Einstein relation can be employed:

$$\frac{D}{\mu} = \frac{k_B T}{e} = \frac{2}{3} \langle u \rangle \quad (14)$$

where e is the unsigned electron charge, k_B is Boltzmann's constant, T is the particle temperature and $\langle u \rangle$ is the characteristic energy of the particle (9:20). This relation becomes very important as many times the ion and background gas temperatures are assumed to be equivalent. Usually taken as $300^\circ K$ or approximately $1/40 eV$, Eq. (14) is used to evaluate the ion diffusion coefficient

$$D_p[E / p] = \frac{1}{40} \mu_p[E / p]. \quad (15)$$

Sources and Sinks

Equally important to the fluid equations are the source/loss terms. Each of these terms involves rate parameters that display the same energy or reduced field dependence seen in the transport coefficients. These terms show up on the right-side of the particle and energy continuity equations – Eqs. (3) and (5). The number of included terms depends heavily on the assumptions of the problem (Appendix A).

The particle continuity equation may include such source/loss processes as ionization, attachment, detachment or recombination. Ionization occurs when an electron impacts a neutral particle above the ionization threshold energy and causes that neutral particle to lose an electron, becoming an ion. This process creates both an electron and an ion and is therefore a source for both the electron and ion continuity equations (20:4):

$$S_{i,e,p} = n_e \nu_i[u_e] \quad (16)$$

In this equation, $\nu_i[u_e]$ represents the ionization frequency based on local average electron energy.

Although not included in this work, two processes associated with an electronegative gas are included for completeness. Detachment occurs when a negative ion suffers a collision that releases its extra electron. This process creates one electron and one neutral particle and therefore factors only into the electron continuity equation as a source:

$$S_{d,e} = k_d n_- n_e . \quad (17)$$

In Eq. (17), k_d is the detachment coefficient and n_- represents the negative ion density (24:4). This interaction in reverse is called attachment. Attachment occurs when an electron attaches to a neutral particle therefore causing the loss of an electron and the gain of a negative ion. This process is modeled as

$$S_{attach,-} = L_{attach,e} = n_e \nu_a \quad (18)$$

where ν_a represents the attachment frequency of the gas (24:4).

Finally, recombination covers two separate processes. The first occurs when an electron recombines with an ion and creates a loss for both particle species (20:4):

$$L_{recomb,e,p} = \beta_{e-i} n_e n_p . \quad (19)$$

where β_{e-i} represents the electron-ion recombination rate. While this rate is usually represented as a constant $\approx 10^{-7} \text{ cm}^3 / \text{s}$, it is actually dependent on the local electron temperature. It is proportional to $T_e^{-1/2}$ for lower gas temperatures (ranging from room temperature up to the thousands of Kelvin) or $T_e^{-3/2}$ for higher gas temperatures (9:60). The second process, ion-ion recombination, occurs when a negative and positive ion collide and form two neutrals. This process causes a loss of both positive and negative ions:

$$L_{recomb,-} = L_{recomb,p} = \beta_{i-i} n_- n_p . \quad (20)$$

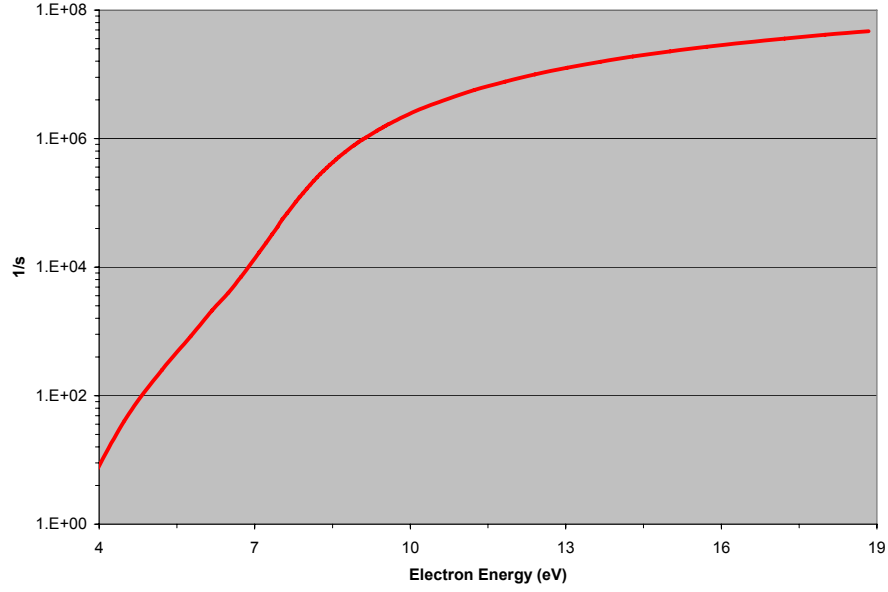


Figure 11. Ionization Frequency in Helium at 1 Torr (17)

Since this project neglects negative ions, the only terms included in the continuity source term will be ionization and recombination. Combining the two creates a continuity source/loss equation of the form

$$S_{e,p} = n_e \nu_i [u_e] - \beta_{e-i} n_e n_p \quad (21)$$

where $S_{e,p}$ represents the source/loss term for both the ion and electron continuity equations. In contrast to the relatively weak dependence on mean energy of the recombination coefficient, the ionization rate for Helium gas varies nearly six orders of magnitude in the energy range 5-18eV (Fig. 11).

The energy source/loss term S_e in Eq. (5) also has production and loss terms.

Joule heating creates a source (20:4):

$$S_{Joule,\varepsilon} = \vec{J} \cdot \vec{E} = -e\vec{\Gamma}_e \cdot \vec{E} \quad (22)$$

where \vec{J} represents the electron current density. Although this number could be negative if the electron flux and electric field are in the same direction, it is more often a positive number and is therefore normally considered a source. A general energy loss term creates the sink (20:4):

$$L_{k_L,\varepsilon} = n_e N k_L [u_e]. \quad (23)$$

where $k_L [u_e]$ is the average energy loss rate dependent on the local average electron energy (14:1377-1378). This rate represents the dissipation of electron energy in collisions with neutrals. The total energy source/loss term becomes

$$S_\varepsilon = -e\vec{\Gamma}_e \cdot \vec{E} - n_e N k_L [u_e]. \quad (24)$$

In order to incorporate the energy loss term into the energy equation, Eq. (5), the energy loss coefficient is expressed in terms of the mean electron energy. This loss coefficient arises from the accumulated energy losses due to elastic and inelastic collisions with neutrals. The energy dependence of the loss coefficient is derived from a solution of the zero dimensional, collisional Boltzmann Equation. To establish the functional dependence of this loss coefficient, consider modeling a homogenous, steady-state plasma with the time and space derivatives in Eq. (5) eliminated and the balance expressed as

$$n_e N k_L [u_e] = -e\vec{\Gamma}_e \cdot \vec{E}. \quad (25)$$

Assuming the electron flux to be only field dependent and substituting part 1 of Eq. (10), this balance equation would be

$$n_e N k_L [u_e] = -e(-\mu_e n_e \vec{E}) \cdot \vec{E}. \quad (26)$$

Rearranging these parameters and eliminating common terms, Eq. (26) becomes

$$k_L [u_e] = e(\mu_e \vec{E}) \cdot \frac{\vec{E}}{N}. \quad (27)$$

Multiplying and dividing the right-hand side by N gives

$$k_L [u_e] = e\mu_e N \cdot \left(\frac{\vec{E}}{N}\right)^2. \quad (28)$$

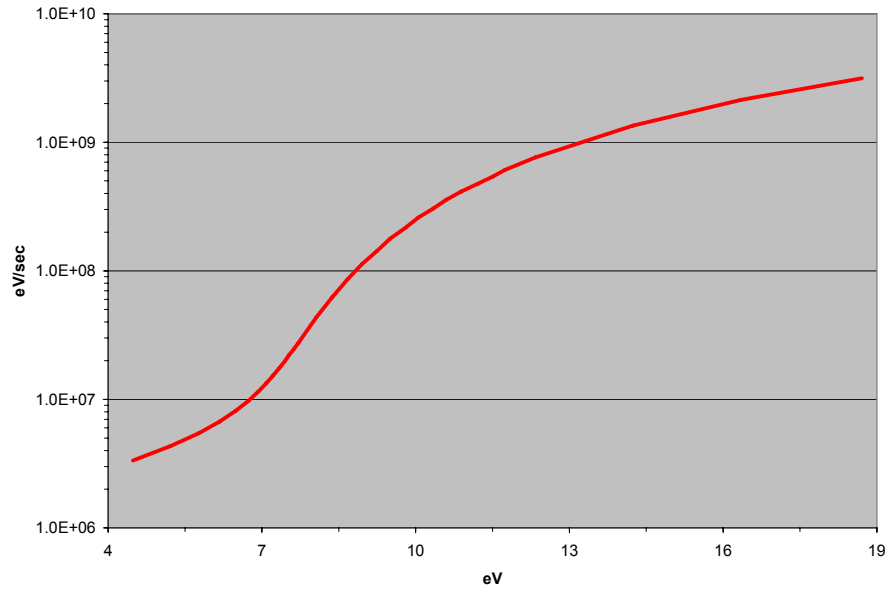


Figure 12. Electron Energy Loss Frequency in Helium (17)

Eq. (28) is expressed in terms of electron charge, electron mobility, neutral number density and the reduced field. Since the mean energy is only a function of the reduced field, the functional dependence of k_L can be inverted to express this term now as a function of mean energy. The resulting energy loss frequency expressed as the loss coefficient multiplied by the neutral number density, $Nk_L[u_e]$, is presented in Fig. 12. Because the energy loss rate increases three orders of magnitude in the range of 5-18eV, care must be taken to get an accurate fit or the numerical results will be faulty.

Poisson's Equation

While the fluid equations, transport coefficients and source/loss rates remain very important to the DBD model, the piece that ties them all together is Poisson's equation. Ultimately, Poisson's equation relates the local charge density to the electric field and the electric potential. In a discharge, this relationship governs discharge characteristics.

The relationship starts with Gauss's Law (21:464):

$$\bar{\nabla} \cdot \bar{D} = \rho \quad (29)$$

or expanded as:

$$\bar{\nabla} \cdot (\epsilon \bar{E}) = q(n_p - n_e) \quad (30)$$

where

$$\bar{E} = -\bar{\nabla} \phi. \quad (31)$$

In these equations, \vec{D} represents the electric displacement, φ is the electric potential and ε is the electric permittivity. It is important to note that the addition of a vector symbol distinguishes electric displacement (\vec{D}) from diffusion coefficient (D).

It is common practice to combine Eqs. (30) and (31) to generate an equation relating the potential directly to the particle densities (25:125)

$$\vec{\nabla} \cdot (\varepsilon \vec{\nabla} \varphi) = -q(n_p - n_e). \quad (32)$$

Assuming that the dielectric constant does not have spatial dependence this equation becomes

$$\varepsilon \nabla^2 \varphi = -q(n_p - n_e). \quad (33)$$

Eq. (33) is known as Poisson's equation. Although Eqs. (29), (30) and (33) are equivalent this final transformation ensures that boundary conditions can be easily implemented. Electric potential is a directly measurable quantity and is chosen as a boundary value both experimentally and numerically. While some problems call for an electric field boundary condition (the dielectric boundary), this is translated into an electric potential condition with Eq. (31).

With this definition of Poisson's equation, each important feature of the fluid approach has been identified and developed. The transport coefficients and source/loss rates have been established:

Electron Mobility	$\mu_e[u_e]$,
Electron Diffusion	$D_e[u_e]$,

Ion Mobility	$\mu_p [E / p],$
Ion Diffusion	$D_p [E / p] = \frac{1}{40} \mu_p [E / p],$
Electron/Ion Source/Loss	$S_e = S_p = n_e \nu_i [u_e] - \beta_{e-i} n_e n_p,$
Energy Source/Loss	$S_\varepsilon = -e \bar{\Gamma}_e \cdot \vec{E} - n_e N k_L [u_e].$

Each of the fluid equations have been defined:

Electron Continuity	$\frac{\partial n_e}{\partial t} + \bar{\nabla} \cdot \bar{\Gamma}_e = S_e,$
Electron Flux	$\bar{\Gamma}_e = -n_e \mu_e \vec{E} - D_e \bar{\nabla} n_e,$
Ion Continuity	$\frac{\partial n_p}{\partial t} + \bar{\nabla} \cdot \bar{\Gamma}_p = S_p,$
Ion Flux	$\bar{\Gamma}_p = n_p \mu_p \vec{E} - D_p \bar{\nabla} n_p,$
Electron Energy	$\frac{\partial (n_e u_e)}{\partial t} + \bar{\nabla} \cdot \bar{\Gamma}_\varepsilon = S_\varepsilon,$
Electron Flux	$\bar{\Gamma}_\varepsilon = -(n_e u_e) \mu_e \vec{E} - D_e \bar{\nabla} (n_e u_e),$
Poisson's Equation	$\bar{\nabla} \cdot (\varepsilon \bar{\nabla} \varphi) = -q (n_p - n_e).$

This system of equations can now be cast onto a grid in order to numerically solve for each of the primary variables φ , n_e , n_p and $(n_e u_e)$.

III. DBD Computational Development

Before a solution to this set of equations is possible, each of the equations must be cast into numerical form. The spatial and flux discretization schemes as well as the boundary conditions will be detailed. The time discretization schemes will be dependent on the type of model implemented.

Table 1. Node and Half Node Values	
Node Values	Half-Node Values
φ	\bar{E}
n_e	\bar{D}
n_p	\bar{v}_e, \bar{v}_p
$n_e u_e$	$\bar{\Gamma}_e, \bar{\Gamma}_p$
μ_e, D_e, μ_p, D_p	$\varepsilon_0, \varepsilon_1$
	$\mu_{e,1/2}, D_{e,1/2}, \mu_{p,1/2}, D_{p,1/2}$

Spatial Discretization

The equations are discretized and cast onto the staggered grid depicted in Fig. (13). The solid circles represent node locations. At each node, the variables appearing the first column of Table 1 are determined. The half-node positions, identified by the x's are shown in the second column of Table 1.

Because the potential and particle densities will be used to specify boundary conditions, the grid is set-up so that there is a node for each boundary and half-nodes exactly half-way between. In Fig. 13, the shaded nodes represent the boundary value

cells. These cells will not be included as part of the computational domain. The domain is labeled with designators ranging from $0 \rightarrow (N-1)$ because the C coding language uses this range for array indices. As an example, Fig. 14 shows the electric potential and electric field indexing scheme as well as the grid spacing.



Figure 13. Grid format

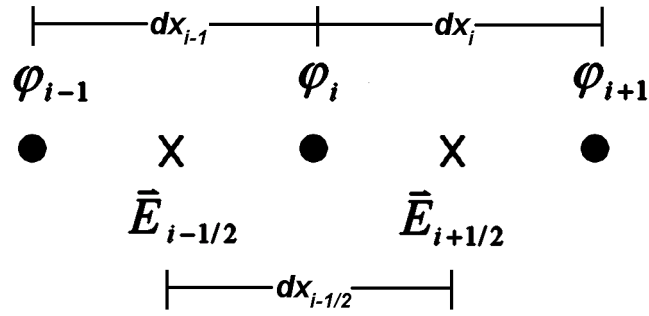


Figure 14. Grid Designation - 'i' Index

In Fig. 14, the grid spacing is equal

$$dx_{i-1} = dx_i = dx_{i-1/2} . \quad (34)$$

The set-up of the computational grid becomes very important to the validity of the numerical results. The location and value of the boundary conditions is integral to the computation. An accurate distinction of half-cell and full cell values in each of the equations is essential to an accurate numerical solution. Finally, the choice of

discretization can make or break the stability of the numerical technique. One example is the Scharfetter-Gummel method for flux discretization.

Scharfetter-Gummel Flux Discretization

Originating in 1969 in a paper addressing Read diodes (26:73), D.L. Scharfetter and H.K. Gummel created an exponential flux representation giving greater stability to the charged particle flux calculations. This exponential weighting scheme more accurately calculates the flux in discharge regimes transitioning between field-dominated and diffusion dominated flux. For DBD applications, the density flux given by Eq. (4) takes the form:

$$\bar{\Gamma}_{s,i+1/2} = \frac{1}{\Delta x} \left[n_{s,i} D_{s,i} \exp(Z_{s,i+1/2}) - n_{s,i+1} D_{s,i+1} \right] \frac{Z_{s,i+1/2}}{\exp(Z_{s,i+1/2}) - 1} \quad (35)$$

where Δx represents the grid spacing and

$$Z_{s,i+1/2} = -\text{sgn}[q] \frac{\mu_{s,i+1/2}}{D_{s,i+1/2}} (\phi_{i+1} - \phi_i) \quad (36)$$

where $\text{sgn}[q]$ represents the charge of the particle type taking on a value of -1 for negatively charged particles and $+1$ for positively charged particles.

For greater clarity in equation development, Eq. (35) will be redefined with substitute variables. Taking

$$F1[Z_{s,i+1/2}] = \frac{\exp(Z_{s,i+1/2}) \cdot Z_{s,i+1/2}}{\exp(Z_{s,i+1/2}) - 1} \quad (37)$$

and

$$F2[Z_{s,i+1/2}] = \frac{Z_{s,i+1/2}}{\exp(Z_{s,i+1/2}) - 1} \quad (38)$$

then Eq. (35) becomes

$$\bar{\Gamma}_{s,i+1/2} = \frac{1}{\Delta x} (n_{s,i} D_{s,i} F1[Z_{s,i+1/2}] - n_{s,i+1} D_{s,i+1} F2[Z_{s,i+1/2}]). \quad (39)$$

Applying this same procedure to the energy flux, Eq. (6) takes the form

$$\bar{\Gamma}_\varepsilon = \frac{1}{\Delta x} ((n_e u_e)_i D_{e,i} F1[Z_{e,i+1/2}] - (n_e u_e)_{i+1} D_{e,i+1} F2[Z_{e,i+1/2}]). \quad (40)$$

Eqs. (39) and (40) will be used for all fluxes in the domain except the boundary flux.

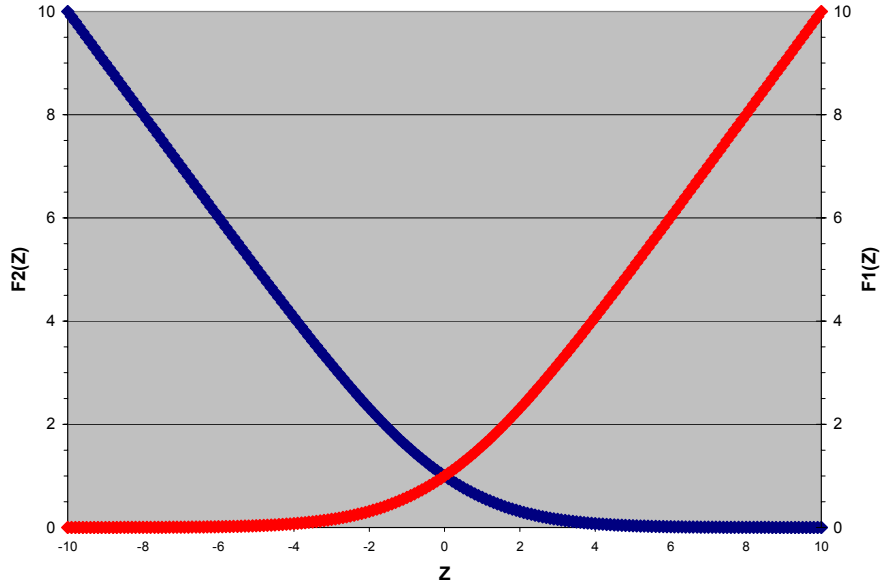


Figure 15. $F1[Z]$ and $F2[Z]$

The utility of the Scharfetter-Gummel flux discretization method can be better described through example. Fig. 15 shows that $F1[Z]$ and $F2[Z]$ are symmetric across the y-axis. Manipulating the discretized form of Eq. (31) yields

$$(\varphi_{i+1} - \varphi_i) = -\bar{E} \cdot \Delta x. \quad (41)$$

Replacing the electric potential term in Eq. (36) we can relate Z directly to \bar{E} as

$$Z_{s,i+1/2} = s \frac{\mu_{s,i+1/2}}{D_{s,i+1/2}} \bar{E}_{i+1/2} \cdot \Delta x. \quad (42)$$

In the diffusion limit of the flux approximation, the field contribution is essentially zero (27:9). From Eq. (42) this means that Z will be approximately zero. In this limit, the F-terms become

$$Z_{i+1/2} \approx 0 \rightarrow (F1[Z_{i+1/2}] \approx F2[Z_{i+1/2}] \approx 1). \quad (43)$$

Now the flux equation becomes

$$\bar{\Gamma}_{i+1/2} = \frac{1}{\Delta x} (n_i D_i - n_{i+1} D_{i+1}). \quad (44)$$

Assuming a spatially constant diffusion coefficient, it can be cast into the familiar equation seen in part 2 of Eq. (10):

$$\bar{\Gamma}_{i+1/2} = -D \left(\frac{n_{i+1} - n_i}{\Delta x} \right). \quad (45)$$

The drift limit of the Scharfetter-Gummel flux can be determined in a similar manner. In this limit, the electric field would be either a large negative or large positive value. The value of Z also becomes either significantly greater than or less than 1. In this regime, one of the F -terms will go to zero (27:9):

$$\text{sgn}[q] \cdot \bar{E} \gg \frac{D_{i+1/2}}{\mu_{i+1/2}} \rightarrow Z_{i+1/2} \gg 1 \rightarrow \begin{pmatrix} F1[Z_{i+1/2}] \rightarrow Z_{i+1/2} \\ F2[Z_{i+1/2}] \rightarrow 0 \end{pmatrix} \quad (46)$$

or

$$\text{sgn}[q] \cdot \bar{E} \ll \frac{D_{i+1/2}}{\mu_{i+1/2}} \rightarrow Z_{i+1/2} \ll 1 \rightarrow \begin{pmatrix} F1[Z_{i+1/2}] \rightarrow 0 \\ F2[Z_{i+1/2}] \rightarrow |Z_{i+1/2}| \end{pmatrix}. \quad (47)$$

Combining Eqs. (39), (42) and (46), the flux becomes

$$\bar{\Gamma}_{i+1/2} = \text{sgn}[q] \cdot n_i \mu_{i+1/2} \bar{E}_{i+1/2}. \quad (48)$$

Combining Eqs. (39), (42) and (47), the flux would be

$$\bar{\Gamma}_{i+1/2} = -\text{sgn}[q] \cdot n_{i+1} \mu_{i+1/2} \bar{E}_{i+1/2}. \quad (49)$$

Eqs. (48) and (49) also help relate how the Scharfetter-Gummel flux discretization is a form of upwinding (27:10). The conditions of Eq. (48) prescribe that $\text{sgn}[q] \cdot \bar{E}_{i+1/2} \gg D_{i+1/2} / \mu_{i+1/2}$. This means that the field must be large *and* the charge of the particle and the polarity of the field are the same. This applies to a negative electric field for electrons and a positive electric field for ions. Under these conditions, the flux at the $i+1/2$ half-node is based on the particle density at node i . If, on the other hand,

the charge of the particle and polarity of the field are opposite, the flux at the $i + 1/2$ half-node is based on the particle density at node $i + 1$. The upwinding process contributes to the stability of the Scharfetter-Gummel flux discretization method. This method is used to calculate all fluxes except the boundary values.

Boundary Conditions

For this project, the flux, potential and particle densities are specified at the boundaries. The boundary particle densities will be treated in two different ways depending on the type of model being implemented. In some cases, the boundary densities were taken to be zero because the boundary cells do not factor into the continuity or flux calculations. In other cases, it is necessary to set the ion density *gradient* equal to zero at the boundary so that the ion boundary flux is field driven only (14:1379). The particular cases to which each specification applies will be covered in the next chapter.

For the electron and energy flux at the boundaries, this code implements a thermal flux with secondary emission for all exposed electrodes. For the electrons, the boundary thermal flux becomes

$$\bar{\Gamma}_{e,1/2} = \bar{\Gamma}_{e,N-1-1/2} = \mp \frac{1}{4} n_e v_{e,th} \quad (50)$$

where $v_{e,th}$ is the electron thermal velocity which can be calculated as

$$v_{e,th} = \sqrt{\frac{8k_B T_e}{\pi \cdot m_e}}, \quad (51)$$

m_e is the electron mass and T_e is the electron temperature (14:1379). The thermal flux is always directed toward the electrode so that the sign in Eq. (50) will be negative for the left electrode and positive for the right. Substituting known values and relating $k_B T_e$ back to the electron average energy this equation becomes

$$v_{e,th} = 4.19 \times 10^5 \sqrt{u_e} . \quad (52)$$

The electron energy flux takes a very similar form (14:1379):

$$\bar{\Gamma}_{\varepsilon,1/2} = \bar{\Gamma}_{\varepsilon,N-1-1/2} = \mp \frac{1}{4} n_e v_{e,th} (k_B T_e) . \quad (53)$$

Again substituting values, this equation relates to the electron energy density as

$$\bar{\Gamma}_{\varepsilon,1/2} = \bar{\Gamma}_{\varepsilon,N-1-1/2} = \mp \frac{1}{3} (n_e u_e) v_{e,th} . \quad (54)$$

The flux from secondary emission captures the flux of electrons being ejected back into the plasma due to ion-electrode impact. This flux is characterized by

$$\bar{\Gamma}_e = -\gamma \bar{\mathcal{A}}_i \quad (55)$$

where γ is defined as the secondary emission coefficient. This coefficient is usually modeled as a constant with values ranging between 0.0 and 0.5 (16:6).

The ion flux at the boundaries is modeled as the Scharfetter-Gummel representation of the flux at that cell. The ion flux to the electrodes is field-driven when

the drift velocity is directed toward the wall and zero otherwise (14:1379). The ion flux toward the electrode becomes

$$\bar{\Gamma}_{p,1/2} = \frac{1}{\Delta x} (F1[Z_{1/2}] - F2[Z_{1/2}]) n_{p,1} D_{p,1} \quad (56)$$

to the left electrode and

$$\bar{\Gamma}_{p,N-3/2} = \frac{1}{\Delta x} (F1[Z_{N-3/2}] - F2[Z_{N-3/2}]) n_{p,N-2} D_{p,N-2} \quad (57)$$

to the right.

For the potential, the boundary conditions simply specify the value of the potential at the electrode. These values vary greatly depending on which test case is being implemented. For each case, however, the potential at the electrodes is held constant for each time step. If a dielectric is covering the electrode, Poisson's calculation must take into account the charge build-up on the dielectric surface.

The Dielectric Boundary

The dielectric configuration used for this project is shown in Fig. 16. Both electrodes and the dielectric barrier are considered to be infinite in transverse extent. While there are several models that could be used to address the charge build-up on the dielectric surface (6:313; 28:167; 29:98), this project will use the method prescribed by Boeuf (14:1379). The dielectric surface is modeled as sticky accumulating all charge

striking its surface. Additionally, this model assumes that once the charges strike the surface, any ion and electron pair recombine instantaneously.

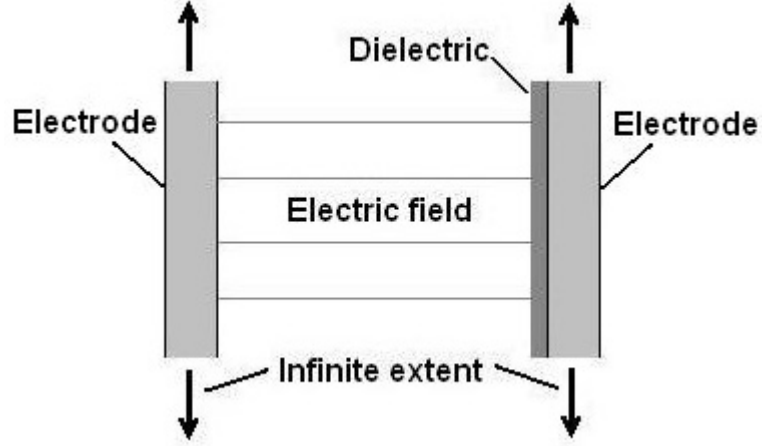


Figure 16. 1-D Dielectric Configuration

The geometry of the dielectric and impinging flux is represented by Fig. 17. The surface charge accumulates as

$$\frac{\partial \sigma_{ds}}{\partial t} = e \left(\left| \bar{\Gamma}_{p,ds-1/2} \right| - \left| \bar{\Gamma}_{e,ds-1/2} \right| \right) \quad (58)$$

where σ_{ds} is the surface charge density accumulated on the dielectric. Because the charges stick to the dielectric surface, they only contribute to the surface charge density and not the individual particle densities n_e and n_p . The particle n_{ds} are zero and the electron flux onto the surface is taken as the thermal flux without secondary emission

$$\bar{\Gamma}_{e,ds-1/2} = \frac{1}{4} n_{e,ds-1} \bar{v}_{e,ds-1/2,th} \quad (59)$$

The ion flux is

$$\bar{\Gamma}_{p,ds-1/2} = \frac{1}{\Delta x} \left(n_{p,ds-1} D_{p,ds-1} F1[Z_{p,ds-1/2}] \right). \quad (60)$$

The charge build-up is ignored in the flux equations but accounted for in Poisson's. At the dielectric surface, Poisson's equation is altered to account for the surface charge. In Fig. 17, the permittivity of the dielectric substance ε_1 modeled to the right of φ_{ds} and left of φ_{ds+1} and the permittivity of free space ε_0 is modeled to the left of φ_{ds} . Starting with the discretized form of Eq. (30)

$$\frac{\varepsilon_1 \bar{E}_{ds+1/2}}{\Delta x_{ds}} - \frac{\varepsilon_0 \bar{E}_{ds-1/2}}{\Delta x_{ds-1}} = q(n_{p,ds} - n_{e,ds}). \quad (61)$$

Upon substituting the potentials and rearranging

$$\frac{\varepsilon_1 \Delta x_{ds-1} \varphi_{ds+1} - (\varepsilon_1 \Delta x_{ds-1} + \varepsilon_0 \Delta x_{ds}) \varphi_{ds} + \varepsilon_0 \Delta x_{ds} \varphi_{ds-1}}{\Delta x_{ds} \Delta x_{ds-1}} = -q(n_{p,ds} - n_{e,ds}) \quad (62)$$

gives Poisson's equation accounting for the surface charge density on the dielectric surface. Now the electric potential can be found throughout the computational domain, to include the dielectric cells, by one of the methods addressed in the Numerical Methods section.

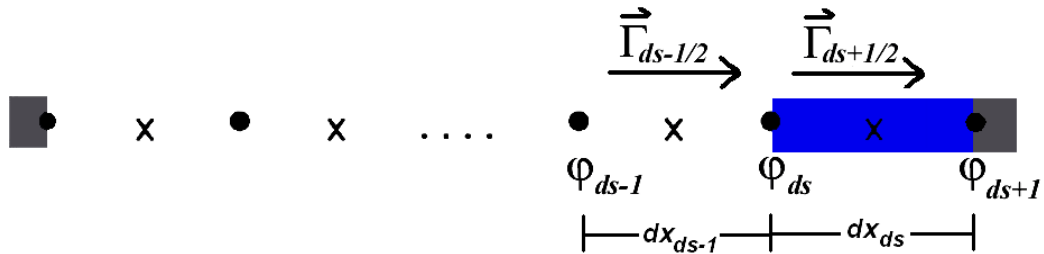


Figure 17. Dielectric Grid Geometry

1-D Numerical Methods

Two different numerical models are used for the calculations in 1-D. The first model involves the sequential solution to Poisson's equation, the electron and ion continuity and the electron energy continuity equations – Eqs. (3), (5) and (33) respectively. The second involves the simultaneous solution to all of these equations. Each of these methods will be covered in detail.

Semi-implicit Sequential

The first numerical model involves a semi-implicit sequential solution to Poisson's equation and the electron, ion and energy continuity equations. The semi-implicit designation indicates that some variables in each equation will be evaluated at the previous time step and others at the current time step. In finite difference form using 'k' as the time index and 'i' as the spatial index, Poisson's equation (non-changing dielectric) becomes

$$\epsilon \frac{\phi_{i-1}^k - 2\phi_i^k + \phi_{i+1}^k}{(\Delta x)^2} = -q(n_{p,i}^k - n_{e,i}^k). \quad (63)$$

Eq. (62) with a time index 'k' on all potential and density variables is the form for the dielectric cell. The electron and ion continuity equations become

$$\frac{n_{e,i}^{k+1} - n_{e,i}^k}{\Delta t} + \frac{\bar{\Gamma}_{e,i+1/2}^{k+1} - \bar{\Gamma}_{e,i-1/2}^{k+1}}{\Delta x} - n_{e,i}^{k+1} \nu_i^k [u_{e,i}^k] + \beta n_{e,i}^{k+1} n_{p,i}^k = 0 \quad (64)$$

and

$$\frac{n_{p,i}^{k+1} - n_{p,i}^k}{\Delta t} + \frac{\bar{\Gamma}_{p,i+1/2}^{k+1} - \bar{\Gamma}_{p,i-1/2}^{k+1}}{\Delta x} + \beta n_{e,i}^{k+1} n_{p,i}^{k+1} = n_{e,i}^{k+1} v_i^k [u_{e,i}^k]. \quad (65)$$

The source term in Eq. (65) must be on the right-hand side because it involves the electron density. This term is still at the advanced time step, however, because the electron continuity calculation is performed first. The flux representation for Eqs. (64) and (65) is

$$\bar{\Gamma}_{e(p),i+1/2}^{k+1} = \frac{1}{\Delta x} \left(n_{e(p),i}^{k+1} D_{e(p),i}^k F1[Z_{e(p),i+1/2}^k] - n_{e(p),i+1}^{k+1} D_{e(p),i+1}^k F2[Z_{e(p),i+1/2}^k] \right) \quad (66)$$

where

$$Z_{e(p),i+1/2} = -\text{sgn}[q] \frac{\mu_{e(p),i+1/2}^k}{D_{e(p),i+1/2}^k} (\phi_{i+1}^k - \phi_i^k). \quad (67)$$

Lastly, the energy density continuity equation looks like

$$\frac{(n_e u_e)_i^{k+1} - (n_e u_e)_i^k}{\Delta t} + \frac{\bar{\Gamma}_{\varepsilon,i+1/2}^{k+1} - \bar{\Gamma}_{\varepsilon,i-1/2}^{k+1}}{\Delta x} = -\bar{\Gamma}_{e,i}^{k+1} \cdot \bar{E}_i^k - n_{e,i}^{k+1} N k_L [u_{e,i}^k] \quad (68)$$

where

$$\bar{\Gamma}_{\varepsilon,i+1/2}^{k+1} = \frac{1}{\Delta x} \left((n_e u_e)_i^{k+1} D_{e,i}^k F1[Z_{e,i+1/2}^k] - (n_e u_e)_{i+1}^{k+1} D_{e,i+1}^k F2[Z_{e,i+1/2}^k] \right). \quad (69)$$

Note that the assumption that all energy quantities are given in eV eliminates the electron charge e originally in Eq. (68).

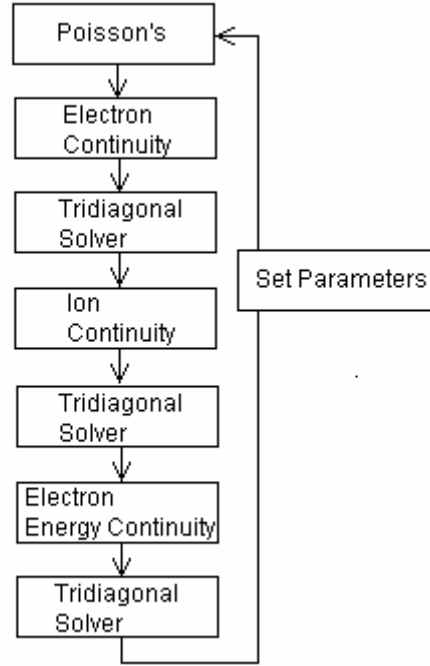


Figure 18. Semi-Implicit Sequential Iterative Scheme

The sequential numerical method solves Eqs. (63), (64), (65) and (68) in succession.

These solutions give the updated values for φ , n_e , n_p and $(n_e u_e)$ respectively. Fig. 18 represents the iterative scheme where one iteration involves the consecutive solutions to Poisson's, electron continuity, ion continuity and electron energy equations.

The iterative scheme for the sequential method is shown in Fig. 18. One iteration involves the consecutive solutions Eqs. (63), (64), (65) and (68). Poisson's equation is solved using an SOR routine while each of the continuity equations is solved using a tridiagonal solver. After each iteration, the reduced field/energy-based rates are reset. The electron mobility and diffusion coefficients as well as the ionization and energy loss rates are set using the updated average electron energy. The ion mobility coefficient is adjusted with the updated reduced field \bar{E}/p and the ion diffusion coefficient is set

using Eq. (15) assuming the ion temperature is approximately equal to the gas temperature at $0.02eV$. Once these parameters are updated, the code recalculates the time step using Eq. (70) and returns to solving the primary equations.

For each iteration, one time step is taken where each time step is limited by the dielectric relaxation time t_{di} where

$$t_{di} = \frac{\epsilon_0}{e(n_e \mu_e + n_p \mu_p)}. \quad (70)$$

This limitation factors in because the sequential solution can not overstep the movement of each of the particles in the continuity equation. The drift portion of the flux equations describes the motion of charged particles in an electric field. Yet it doesn't take into account variations in the electric field as each of the particles moves (15:5609). If a time step is taken that exceeds the dielectric relaxation time, the particles move enough to significantly alter the electric field and the field driving their motion becomes invalid. If this occurs too often, the code quickly becomes unstable causing either a crash or inaccurate results. The key to stability lies in an accurate, updated solution to Poisson's equation using the SOR algorithm.

SOR

The method of successive overrelaxation (SOR) is based on the Gauss-Seidel iterative algorithm. Both algorithms are explained in depth in several computational texts (30:863-869; 31:192-194; 32:162-166). For this project, the SOR algorithm was implemented as a root solving routine where Eq. (63) takes the form of

$$\underbrace{\varphi_{i-1}^k - 2\varphi_i^k + \varphi_{i+1}^k}_1 + \underbrace{\frac{q}{\varepsilon}(\Delta x)^2(n_{p,i}^k - n_{e,i}^k)}_2 = 0. \quad (71)$$

Assuming that we currently know all of the variables in part 2 of Eq. (71), the goal is to find out what values of φ_{i-1}^k , φ_i^k , and φ_{i+1}^k make this equation true for all spatial grid points $i = 1, 2, \dots, N - 2$. The first step is to guess values for the potential for the first iteration, call these values $\varphi_i^{old,k}$. Next, solve for an updated $\varphi_i^{*,k}$ using these guess values:

$$\varphi_i^{*,k} = \frac{1}{2} \left[-\varphi_{i-1}^{old,k} - \varphi_{i+1}^{old,k} - \frac{q}{\varepsilon}(\Delta x)^2(n_{p,i}^k - n_{e,i}^k) \right]. \quad (72)$$

Now take a weighted sum of the old and the updated potentials and designate the new value of the electric potential:

$$\varphi_i^{new,k} = \omega \varphi_i^{*,k} + (1 - \omega) \varphi_i^{old,k} \quad (73)$$

where ω is the weighting parameter. The value of the weighting parameter that gives the fastest convergence (32:166-167) is found by solving

$$\omega_{opt} = \frac{2 - 2\sqrt{1 - \left(\cos\left(\frac{\pi}{N-1}\right)\right)^2}}{\left(\cos\left(\frac{\pi}{N-1}\right)\right)^2} \quad (74)$$

where ω_{opt} is the optimal weighting parameter to achieve the fastest convergence.

Finally, check the convergence. For this code, the convergence criteria was $\varsigma \leq 1e-5$

where

$$\varsigma = \sum_{i=1}^{N-2} \left\{ \left| \frac{\varphi_i^{k,old} - \varphi_i^{k,new}}{\varphi_i^{k,new}} \right| \xrightarrow{\text{for}} \varphi_i^{k,new} > 1 \right\}. \quad (75)$$

Cycle through Eqs. (72), (73) and (75) for all spatial values until the convergence criteria is reached. At this point, the electric potential contained in the ‘new’ array is taken to be the value of the potential for the current time step. This potential is used to solve for the electric field which is used for the remainder of the semi-implicit iteration to solve the fluid equations. For the semi-implicit method, all the potentials are values from the previous iteration because they are simply accounting for the density changes that occurred during the last cycle.

Tridiagonal

The fluid equations will be solved using a generalized Thomas Algorithm (33). This algorithm is commonly used as an efficient solver for systems of equations that can be cast into tridiagonal form. With a little manipulation, all of the fluid equations can be formatted as tridiagonal systems of equations. Using the electrons as an example, first combine Eqs. (64) and (66) to give

$$\begin{aligned}
& \frac{n_{e,i}^{k+1} - n_{e,i}^k}{\Delta t} + \frac{\frac{1}{\Delta x} \left(n_{e,i}^{k+1} D_{e,i}^k F1[Z_{e,i+1/2}^k] - n_{e,i+1}^{k+1} D_{e,i+1}^k F2[Z_{e,i+1/2}^k] \right)}{\Delta x} \\
& - \frac{\frac{1}{\Delta x} \left(n_{e,i-1}^{k+1} D_{e,i-1}^k F1[Z_{e,i-1/2}^k] - n_{e,i}^{k+1} D_{e,i}^k F2[Z_{e,i-1/2}^k] \right)}{\Delta x} - n_{e,i}^{k+1} \nu_i^k [u_{e,i}^k] + \beta n_{e,i}^{k+1} n_{p,i}^k = 0
\end{aligned} \quad (76)$$

Multiplying through by $\Delta t \cdot (\Delta x)^2$ and rearranging terms, this equation becomes

$$\begin{aligned}
& n_{e,i-1}^{k+1} \left(-\Delta t \cdot D_{e,i-1}^k F1[Z_{e,i-1/2}^k] \right) + \\
& n_{e,i}^{k+1} \left((\Delta x)^2 + \Delta t \cdot D_{e,i}^k F1[Z_{e,i+1/2}^k] + \Delta t \cdot D_{e,i}^k F2[Z_{e,i-1/2}^k] \right) + \\
& \left(-(\Delta x)^2 \Delta t \cdot \nu_i^k [u_{e,i}^k] + (\Delta x)^2 \Delta t \cdot \beta n_{p,i}^k \right) + \\
& n_{e,i+1}^{k+1} \left(-\Delta t \cdot D_{e,i+1}^k F2[Z_{e,i+1/2}^k] \right) \\
& = n_{e,i}^k (\Delta x)^2
\end{aligned} \quad (77)$$

This equation is now in tridiagonal form. Taking the coefficients of the discretized electron densities at the node locations $n_{e,i-1}$, $n_{e,i}$ and $n_{e,i+1}$ and associating them with l_i , d_i and u_i , then designating the known variables of the right-hand side to equal f_i this equation looks like

$$n_{e,i-1}^{k+1} (l_i) + n_{e,i}^{k+1} (d_i) + n_{e,i+1}^{k+1} (u_i) = f_i. \quad (78)$$

The coupled equations can take on the matrix form $Ax = b$:

$$\begin{array}{c}
\overbrace{\begin{bmatrix} d_1 & u_1 & 0 & 0 & 0 & \dots \\ l_2 & d_2 & u_2 & 0 & 0 & \dots \\ 0 & l_3 & d_3 & u_3 & 0 & \dots \\ \dots & \dots & \dots & \dots & \dots & \dots \\ 0 & 0 & 0 & l_{N-3} & d_{N-3} & u_{N-3} \\ 0 & 0 & 0 & 0 & l_{N-2} & d_{N-2} \end{bmatrix}}^A \overbrace{\begin{bmatrix} n_{e,1}^{k+1} \\ n_{e,2}^{k+1} \\ n_{e,3}^{k+1} \\ \vdots \\ n_{e,N-3}^{k+1} \\ n_{e,N-2}^{k+1} \end{bmatrix}}^x = \overbrace{\begin{bmatrix} f_1 \\ f_2 \\ f_3 \\ \vdots \\ f_{N-3} \\ f_{N-2} \end{bmatrix}}^b.
\end{array} \quad (79)$$

In this equation, A is the $(N-2) \times (N-2)$ coefficient matrix for the electron density at the current time step, x is the vector of unknown electron densities at the current time step and b is vector of known values consisting of the electron density at the previous time step and the ionization source term. Now the generalized Thomas algorithm can be easily implemented to solve this system of equations for the electron density at the next time step.

The ion and energy continuity equations are manipulated in the same manner used to create Eq. (77). Moving the source term to the right-hand side and changing all other particle densities to ions, the ion continuity equation is identical to Eq. (77). The energy density becomes

$$\begin{aligned}
& (n_e u_e)_{i-1}^{k+1} \left(-\frac{5}{3} \Delta t \cdot D_{e,i-1}^k F1[Z_{e,i-1/2}^k] \right) + \\
& (n_e u_e)_i^{k+1} \left((\Delta x)^2 + \frac{5}{3} \Delta t \cdot D_{e,i}^k F1[Z_{e,i+1/2}^k] + \frac{5}{3} \Delta t \cdot D_{e,i}^k F2[Z_{e,i-1/2}^k] \right) + \\
& (n_e u_e)_{i+1}^{k+1} \left(-\frac{5}{3} \Delta t \cdot D_{e,i+1}^k F2[Z_{e,i+1/2}^k] \right) \\
& = (n_e u_e)_i^k (\Delta x)^2 - \bar{\Gamma}_{e,i}^{k+1} \cdot \bar{E}_i^k - n_{e,i}^{k+1} N k_L [u_{e,i}^k]
\end{aligned} \quad (80)$$

Using the new values for the l_i , d_i , u_i and f_i coefficients, the same tridiagonal method is used to solve for the advanced time step ion and energy densities.

Semi-Implicit Summary

Overall, the semi-implicit sequential method is relatively easy to code and gives accurate results as long as the time step remains within the dielectric relaxation time. This time step, however, was determined to be a constraint for goals of this project. As Eq. (70) relates, the dielectric relaxation time is inversely proportional to the particle densities. This time step significantly diminishes with nearly any increase in the charge densities.

As an example, helium gas at 1 torr with an assumed initial charge density of $1 \times 10^{15} m^{-3}$ (an ionization fraction on the order of 1×10^{-7}) has a dielectric relaxation time $\approx 0.15 ns$ before any growth due to ionization is taken into account. If the goal is to cover one cycle of an RF discharge with a 10MHz frequency, it would only require around 670 iterations. If the goal is a steady-state solution (~ 500 cycles), however, this time step becomes a serious hindrance. This is why the fully-implicit simultaneous numerical method is the next step. This method allows a larger time step which greatly enhances the modeling power of the code.

Fully Implicit Simultaneous

The second numerical model involves a fully implicit, simultaneous solution to Poisson's equation and the electron, ion and energy continuity equations. 'Fully implicit' indicates that the values for all potentials, particle densities, energy densities and source/loss rates will be evaluated at the advanced time. This algorithm becomes more

involved than the sequential method because it must address the non-linear nature of the coupled system of equations.

The finite difference form of these equations utilizes the Crank-Nicholson method for stabilization and the Newton-Raphson method to linearize and solve the system. For this section, the designation of the iteration and time variables are changed significantly. An ‘m’ designates the *previous* time step, ‘m+1’ the current time step, ‘k’ the previous iteration and ‘k+1’ the current iteration.

Crank-Nicholson

The Crank-Nicholson method is an implicit technique that provides second order accuracy in both time and space dimensions (34:841). This method uses the average of the flux at the previous time step m and the current time step $m + 1$ to replace the divergence term in the continuity equations. The Crank-Nicholson differenced forms of Eqs. (3) and (5) become

$$\frac{n_{e(p)i}^{m+1} - n_{e(p)i}^m}{\Delta t} + \frac{1}{2} \left(\frac{\bar{\Gamma}_{e(p),i+1/2}^{m+1} - \bar{\Gamma}_{e(p),i-1/2}^{m+1}}{\Delta x} + \frac{\bar{\Gamma}_{e(p),i+1/2}^m - \bar{\Gamma}_{e(p),i-1/2}^m}{\Delta x} \right) = n_{e,i}^m V_i [u_{e,i}^{m+1}] \quad (81)$$

and

$$\begin{aligned} & \frac{(n_e u_e)_i^{m+1} - (n_e u_e)_i^m}{\Delta t} + \frac{1}{2} \left(\frac{\bar{\Gamma}_{\varepsilon,i+1/2}^{m+1} - \bar{\Gamma}_{\varepsilon,i-1/2}^{m+1}}{\Delta x} + \frac{\bar{\Gamma}_{\varepsilon,i+1/2}^m - \bar{\Gamma}_{\varepsilon,i-1/2}^m}{\Delta x} \right) \\ & = -\bar{\Gamma}_{e,i}^m \cdot \bar{E}_i^m - n_{e,i}^m N k_L [u_{e,i}^{m+1}] \end{aligned} \quad (82)$$

As the time step is increased, this averaging method adds needed stability to the system of highly non-linear equations. In order to solve the equations, the Newton-Raphson algorithm is employed.

Newton-Raphson

In its simplest form, the Newton-Raphson method is a root-finding algorithm (34:147-151). For the purpose of the project, however, it is used as a technique to solve systems of non-linear equations. While McGrath (35) gives an excellent introduction to the Newton-Raphson method as well as a simple, clear example of how it can be used, some of the basics will be covered as they apply to this project.

Before beginning a discussion, it is important to recall some of the basic attributes of the system of equations. The four primary equations of interest are Poisson's equation, the electron continuity, ion continuity and energy continuity equations. The four variables are φ_i , $n_{e,i}$, $n_{p,i}$ and $(n_e u_e)_i$.

The Newton-Raphson algorithm starts by assuming that the variable at the next time step will be equal to the value of the variable at the current iteration plus some delta value. Using the four variables as examples, this means that

$$\begin{aligned}\varphi_i^{k+1,m+1} &= \varphi_i^{k,m+1} + \delta\varphi_i^{k,m+1} \\ n_{e,i}^{k+1,m+1} &= n_{e,i}^{k,m+1} + \delta n_{e,i}^{k,m+1} \\ n_{p,i}^{k+1,m+1} &= n_{p,i}^{k,m+1} + \delta n_{p,i}^{k,m+1} \\ (n_e u_e)_i^{k+1,m+1} &= (n_e u_e)_i^{k,m+1} + \delta (n_e u_e)_i^{k,m+1}\end{aligned}\tag{83}$$

where the δ terms are the corrections to the variables for this time step but the previous iteration. As a quick reminder, $k+1, m+1$ indicates the current time step and current

iteration, $k, m + 1$ indicates the current time step and previous iteration. Any variable at $k + 1, m + 1$ can be approximated in this way as long as the variable is linear. The process becomes slightly more complicated for the non-linear variables.

Using the electron flux at the ‘ $i+1/2$ ’ spatial location as an example, it is easy to see from Eqs. (36) and (39) that the flux is dependent on the electron density and the electric potential at ‘ i ’ and ‘ $i+1$ ’ spatial locations. For this equation, the changes to the flux must account for these four dependencies. The flux correction is still represented as

$$\Gamma_{e,i+1/2}^{k+1,m+1} = \Gamma_{e,i+1/2}^{k,m+1} + \delta \Gamma_{e,i+1/2}^{k,m+1} \quad (84)$$

but the δ value becomes

$$\begin{aligned} \delta \Gamma_{e,i+1/2}^{k,m+1} [n_{e,i+1}, n_{e,i}, \varphi_{i+1}, \varphi_i] = & \left(\frac{\partial \Gamma_{e,i+1/2}^{k,m+1}}{\partial n_{e,i+1}} \right) \delta n_{e,i+1} + \left(\frac{\partial \Gamma_{e,i+1/2}^{k,m+1}}{\partial n_{e,i}} \right) \delta n_{e,i} \\ & + \left(\frac{\partial \Gamma_{e,i+1/2}^{k,m+1}}{\partial \varphi_{i+1}} \right) \delta \varphi_{i+1} + \left(\frac{\partial \Gamma_{e,i+1/2}^{k,m+1}}{\partial \varphi_i} \right) \delta \varphi_i. \end{aligned} \quad (85)$$

In this equation the, the total δ for the flux is the sum of the δ ’s of each of the constituent variables times their partial derivatives. This same method is used for all the non-linear terms in the equations.

Now using the electron continuity equation as an example, the entire Newton-Raphson development will be covered. To begin, Eq. (3) will be written in implicit form with a Crank-Nicholson representation of the flux term:

$$\frac{n_{e,i}^{k+1,m+1} - n_{e,i}^{k,m}}{\Delta t} + \frac{1}{2} \left(\frac{\bar{\Gamma}_{e,i+1/2}^{k+1,m+1} - \bar{\Gamma}_{e,i-1/2}^{k+1,m+1}}{\Delta x} + \frac{\bar{\Gamma}_{e,i+1/2}^{k,m} - \bar{\Gamma}_{e,i-1/2}^{k,m}}{\Delta x} \right) = n_{e,i}^{k,m} v_i [u_{e,i}^{k+1,m+1}]. \quad (86)$$

Moving each of the variables to the left-hand side, this equation can be cast into root solving form. Multiplying by Δt , Eq. (86) becomes

$$NE[\varphi, n_e, (n_e u_e)] = \frac{n_{e,i}^{k+1,m+1} - n_{e,i}^{k,m}}{\Delta t} + \frac{1}{2} \left(\frac{\bar{\Gamma}_{e,i+1/2}^{k+1,m+1} - \bar{\Gamma}_{e,i-1/2}^{k+1,m+1}}{\Delta x} + \frac{\bar{\Gamma}_{e,i+1/2}^{k,m} - \bar{\Gamma}_{e,i-1/2}^{k,m}}{\Delta x} \right) - n_{e,i}^{k,m} v_i [u_{e,i}^{k+1,m+1}] = 0 \quad (87)$$

where $NE[\varphi, n_e, n_e \varepsilon_i]$ represents the total electron equation in root-solving form. Next, all terms at the current time step and current iteration are substituted with their linear equivalents:

$$NE[\varphi, n_e, (n_e u_e)] = (n_{e,i}^{k,m+1} + \delta n_{e,i}^{k,m+1}) - n_{e,i}^{k,m} + \frac{\Delta t}{2\Delta x} \left((\Gamma_{e,i+1/2}^{k,m+1} + \delta \Gamma_{e,i+1/2}^{k,m+1}) - (\Gamma_{e,i-1/2}^{k,m+1} + \delta \Gamma_{e,i-1/2}^{k,m+1}) + \Gamma_{e,i+1/2}^{k,m} - \Gamma_{e,i-1/2}^{k,m} \right) - \Delta t \left(v \left[\frac{(n_e u_e)_i^{k,m+1}}{n_{e,i}^{k,m+1}} \right] + \delta v \left[\frac{(n_e u_e)_i^{k,m+1}}{n_{e,i}^{k,m+1}} \right] \right) * n_{e,i}^{k,m+1} = 0 \quad (88)$$

Understanding that both flux terms and the ionization rate are non-linear terms, in addition to Eq. (85) the following values will be substituted:

$$\delta \Gamma_{e,i-1/2}^{k,m+1} [n_{e,i}, n_{e,i-1}, \varphi_i, \varphi_{i-1}] = \left(\frac{\partial \Gamma_{e,i-1/2}^{k,m+1}}{\partial n_{e,i}} \right) \delta n_{e,i} + \left(\frac{\partial \Gamma_{e,i-1/2}^{k,m+1}}{\partial n_{e,i-1}} \right) \delta n_{e,i-1} + \left(\frac{\partial \Gamma_{e,i-1/2}^{k,m+1}}{\partial \varphi_i} \right) \delta \varphi_i + \left(\frac{\partial \Gamma_{e,i-1/2}^{k,m+1}}{\partial \varphi_{i-1}} \right) \delta \varphi_{i-1} \quad (89)$$

and

$$\begin{aligned}
\delta v \left[\frac{(n_e u_e)_i^{k,m+1}}{n_{e,i}^{k,m+1}} \right] &= \\
\left(\frac{\partial v_i^{k,m+1}}{\partial \langle u_e \rangle_i^{k,m+1}} \right) \left(\frac{\partial \langle u_e \rangle_i^{k,m+1}}{\partial (n_e u_e)_i^{k,m+1}} \right) \delta (n_e u_e)_i^{k,m+1} &+ \left(\frac{\partial v_i^{k,m+1}}{\partial \langle u_e \rangle_i^{k,m+1}} \right) \left(\frac{\partial \langle u_e \rangle_i^{k,m+1}}{\partial n_{e,i}^{k,m+1}} \right) \delta n_{e,i}^{k,m+1} . \quad (90) \\
&= \left(\frac{\partial v_i^{k,m+1}}{\partial \langle u_e \rangle_i^{k,m+1}} \right) \left(\frac{1}{n_{e,i}^{k,m+1}} \right) \delta (n_e u_e)_i^{k,m+1} + \left(\frac{\partial v_i^{k,m+1}}{\partial \langle u_e \rangle_i^{k,m+1}} \right) \left(\frac{-(n_e u_e)_i^{k,m+1}}{(n_{e,i}^{k,m+1})^2} \right) \delta n_{e,i}^{k,m+1}
\end{aligned}$$

Simplifying and rearranging, this equation becomes

$$\begin{aligned}
NE[\varphi, ne, (n_e u_e)_i] &= -\frac{\Delta t}{2\Delta x} \left(\frac{\partial \Gamma_{e,i-1/2}^{k,m+1}}{\partial \varphi_{i-1}} \right) \delta \varphi_{i-1}^{k,m+1} - \frac{\Delta t}{2\Delta x} \left(\frac{\partial \Gamma_{e,i-1/2}^{k,m+1}}{\partial n_{e,i-1}} \right) \delta n_{e,i-1}^{k,m+1} \\
&+ \frac{\Delta t}{2\Delta x} \left(\left(\frac{\partial \Gamma_{e,i+1/2}^{k,m+1}}{\partial \varphi_i} \right) - \left(\frac{\partial \Gamma_{e,i-1/2}^{k,m+1}}{\partial \varphi_i} \right) \right) \delta \varphi_i^{k,m+1} \\
&+ \left(1 + \frac{\Delta t}{2\Delta x} \left(\frac{\partial \Gamma_{e,i+1/2}^{k,m+1}}{\partial n_{e,i}} \right) - \frac{\Delta t}{2\Delta x} \left(\frac{\partial \Gamma_{e,i-1/2}^{k,m+1}}{\partial n_{e,i}} \right) \right. \\
&\quad \left. - \Delta t \left(\frac{\partial v_i^{k,m+1}}{\partial \langle u_e \rangle_i^{k,m+1}} \right) \left(\frac{-(n_e u_e)_i^{k,m+1}}{(n_{e,i}^{k,m+1})^2} \right) \cdot n_{e,i}^{k,m+1} \right) \delta n_{e,i}^{k,m+1} \\
&- \Delta t \left(\frac{\partial v_i^{k,m+1}}{\partial \langle u_e \rangle_i^{k,m+1}} \right) \left(\frac{1}{n_{e,i}^{k,m+1}} \right) (n_{e,i}^{k,m+1}) \delta (n_e u_e)_i^{k,m+1} \\
&+ n_{e,i}^{k,m+1} - n_{e,i}^{k,m} + \frac{\Delta t}{2\Delta x} \left(\frac{\partial \Gamma_{e,i+1/2}^{k,m+1}}{\partial \varphi_{i+1}} \right) \delta \varphi_{i+1}^{k,m+1} + \frac{\Delta t}{2\Delta x} \left(\frac{\partial \Gamma_{e,i+1/2}^{k,m+1}}{\partial n_{e,i+1}} \right) \delta n_{e,i+1}^{k,m+1} \\
&+ \frac{\Delta t}{2\Delta x} \left((\Gamma_{e,i+1/2}^{k,m+1} - \Gamma_{e,i-1/2}^{k,m+1}) + (\Gamma_{e,i+1/2}^{k,m} - \Gamma_{e,i-1/2}^{k,m}) \right) - \Delta t \left(v \left[\frac{(n_e u_e)_i^{k,m+1}}{n_{e,i}^{k,m+1}} \right] \right) n_{e,i}^{k,m+1} = 0 . \quad (91)
\end{aligned}$$

This process is repeated for the remaining three equations. The original and final Newton-Raphson form of the remaining three equations can be found in Appendix B.

The system of equations is now linear and can be cast into the matrix form

$Ax = b$. This matrix equation looks like:

$$\begin{bmatrix} A_1 & B_1 & 0 & 0 & \dots & 0 \\ C_2 & A_2 & B_2 & 0 & \dots & 0 \\ 0 & C_3 & A_3 & B_3 & \dots & 0 \\ \dots & \dots & \dots & \dots & \dots & \dots \\ 0 & \dots & 0 & C_{N-3} & A_{N-3} & B_{N-3} \\ 0 & \dots & 0 & 0 & C_{N-2} & A_{N-2} \end{bmatrix}^{k,m+1} \begin{bmatrix} x_1 \\ x_2 \\ x_3 \\ \dots \\ x_{N-3} \\ x_{N-2} \end{bmatrix}^{k,m+1} = \begin{bmatrix} b_1 \\ b_2 \\ b_3 \\ \dots \\ b_{N-3} \\ b_{N-2} \end{bmatrix}^{k,m+1} \quad (92)$$

where A_n , B_n and C_n are 4x4 sub-matrices, or blocks, consisting of the coefficients of the δ terms, x_n is a four-term sub-vector of the unknown δ 's and b_n is a four-term sub-vector of the variables not involving a δ . Looking at just one submatrix equation shows

$$A_1 = \begin{bmatrix} \frac{\partial(PHI_1)}{\partial\varphi_1} & \frac{\partial(PHI_1)}{\partial n_{e,1}} & \frac{\partial(PHI_1)}{\partial n_{p,1}} & \frac{\partial(PHI_1)}{\partial(n_e u_e)_1} \\ \frac{\partial(NP_1)}{\partial\varphi_1} & \frac{\partial(NP_1)}{\partial n_{e,1}} & \frac{\partial(NP_1)}{\partial n_{p,1}} & \frac{\partial(NP_1)}{\partial(n_e u_e)_1} \\ \frac{\partial(EN_1)}{\partial\varphi_1} & \frac{\partial(EN_1)}{\partial n_{e,1}} & \frac{\partial(EN_1)}{\partial n_{p,1}} & \frac{\partial(EN_1)}{\partial(n_e u_e)_1} \end{bmatrix}^{k,m+1} \begin{bmatrix} \delta\varphi_1 \\ \delta n_{e,1} \\ \delta n_{p,1} \\ \delta(n_e u_e)_1 \end{bmatrix}^{k,m+1} = \begin{bmatrix} PHI(\bar{\delta}) \\ NE(\bar{\delta}) \\ NP(\bar{\delta}) \\ EN(\bar{\delta}) \end{bmatrix}^{k,m+1} \quad (93)$$

where PHI , NE , NP and EN represent the total root-solving representation of each of the variable equations and $PHI(\bar{\delta})$, $NE(\bar{\delta})$, $NP(\bar{\delta})$ and $EN(\bar{\delta})$ represent the terms in each equation that do not involve delta values. For each of the coefficients of the sub-matrices as well as the non-delta terms, see Appendix B. Now the Newton-Raphson linearization is complete.

From here, the problem becomes an iterative root solving routine for a system of *linear* equations. For each time step, the total coefficient matrix is solved for the unknown δ 's. These δ 's are added to the variables at the current time step but previous iteration. This updates the variables for the current time step and current iteration:

$$\begin{aligned}
\phi_i^{k+1,m+1} &= \phi_i^{k,m+1} + \delta\phi_i^{k,m+1} \\
n_{e,i}^{k+1,m+1} &= n_{e,i}^{k,m+1} + \delta n_{e,i}^{k,m+1} \\
n_{p,i}^{k+1,m+1} &= n_{p,i}^{k,m+1} + \delta n_{p,i}^{k,m+1} \\
(n_e u_e)_i^{k+1,m+1} &= (n_e u_e)_i^{k,m+1} + \delta (n_e u_e)_i^{k,m+1}
\end{aligned} \tag{94}$$

Ideally, the roots of the primary equations are found when all of the δ 's go to zero. It is considered adequate, however, that all of the δ values be less than some tolerance that is significantly less than one. For this project taking each of the variables as x , the tolerance was $\varsigma < 1e-5$ where

$$\varsigma = \left\{ \begin{array}{l} \left| \frac{\delta x}{x} \right| \xrightarrow{\text{for}} x > 1 \\ \left| \delta x \right| \xrightarrow{\text{for}} x \leq 1 \end{array} \right\} \tag{95}$$

When this condition is met, the next time step is taken. The last converged solution is used as an initial guess for the next solution. This root solving routine is repeated until the desired total time or number of time iterations is reached.

Fully Implicit Summary

When all of the primary equations are solved simultaneously, the time step constraint given by Eq. (70) relaxes significantly. Each of the variables takes the same time step concurrently and there is no particle motion that is not accounted for by

Poisson's equation. Additionally, the Crank-Nicholson method adds stability and allows for an even greater time step. For the ambipolar test case, for example, while the semi-implicit method was limited to time steps between $0.1 - 1ns$, the fully implicit method allowed a time step on the order of $0.1\mu s$, two to three orders of magnitude greater.

Still this algorithm is not without limitations. While the Newton-Raphson method provides a powerful tool for linearization and solution of these systems of equations, it is limited by the requirement that the initial guess be adequately close to the true solution. Typically, the solution on the previous time step is used as an initial guess for the current time step. In order for the solution to converge, there still must be some limit on the time step based on the needed accuracy of the initial guess.

This is especially true for modeling cases where the sheath region plays a significant role. In these test cases, the electric field is large near the cathode and the electron particle densities change quickly. If the time step is too large, the conditions change too much for the previous solution to provide a satisfactory guess for the next solution. While there is still an increase in the allowed time step, it is not as significant as the ambipolar case. Each of these test cases is covered in detail in the following chapter.

IV. Computational Validation and DBD Results

In order to accurately characterize the DBD in one-dimension, the numerical model must be extensively tested to ensure that the code produces expected results. The semi-implicit numerical model was checked against a variety of analytic and previously validated test cases before the DBD characterization tests were run. Because of difficulties implementing the energy equation into the fully implicit model, only the ambipolar test case was accomplished. In each test, the spatial domain was divided into 101 cells – 99 computational and 2 electrode boundary cells. Unless otherwise specified, the length of the cavity is 0.04m, the electron boundary flux is thermal with secondary emission according to Eqs. (52) and (55) and energy density boundary flux is thermal according to Eq. (54).

Validation

The validation test cases include an analytic examination of Poisson's equation, transient sheath analysis, ambipolar analytic comparison as well as a radio-frequency comparison to previously validated results. Each of these tests is covered in detail below. Several of the analytic comparisons are listed in terms of relative error. Taking 'x' to be the variable of interest this relative error would be:

$$\%error = \left| \frac{x_{analytic} - x_{computational}}{x_{analytic}} \right| \times 100\% . \quad (96)$$

If the results are in array format and will be compared across an entire domain, the errors will be the average % error where

$$avg_ \%error = \frac{\sum_{i=1}^{N-2} \left| \frac{x_{analytic} - x_{computational}}{x_{analytic}} \right| \times 100\%}{N - 2} . \quad (97)$$

Analytic Poisson

An accurate solution to the DBD problem hinges on an accurate solution to Poisson's equation. The first test case was a comparison of the computational results with an analytic solution of Poisson's equation. This test was run for both the semi-implicit and fully implicit numerical schemes and included only the Poisson solver.

First, all charge densities were eliminated and a potential was applied to the right and left electrodes. For this test case, the analytic solution shows a linear dependence of the electric potential on x :

$$\varphi(x) = \frac{\varphi_L - \varphi_0}{L} x + \varphi_0 \quad (98)$$

where φ_0 is the electric potential at the left electrode, φ_L is and electric potential at the right electrode, L is the electrode separation and x is the domain location referenced from the left electrode for this project. Test cases were run with $-500V$, $-10V$ and $100V$ applied to the left electrode and respectively $0V$, $10V$ and $-305V$ applied to the right electrode. Both methods quickly reached the convergence criteria of $1.0e-5$. Convergence was determined by Eqs. (72) and (95) for the semi-implicit and fully implicit methods respectively.

Next, a uniform charge density is distributed throughout the computational domain. Assuming this charge density is some ρ_1 , the analytic solution to this test case is the simple quadratic

$$\varphi(x) = \rho_1 x^2 + \frac{\varphi_L - \varphi_0 - \rho_1 L^2}{L} x + \varphi_0. \quad (99)$$

The same three voltage configurations were tested with net positive and negative charge densities. Again, both solvers quickly reached the convergence criteria. The solution to the first test case for both the zero and constant charge densities are shown in Fig. 19.

The final check on the Poisson solvers involved the insertion of various dielectrics each with a different permittivity. Once again, a test with no charge density and constant charge density was performed. These test cases were checking for the continuity of \vec{D} at the dielectric surface:

$$\vec{D}_1 = \vec{D}_2 \quad (100)$$

or

$$\varepsilon_1 \vec{E}_1 = \varepsilon_2 \vec{E}_2 \quad (101)$$

where the ‘1’ subscript will designate quantities to the left and a subscript ‘2’ will designate quantities to the right of the dielectric change. Both the semi-implicit and fully implicit solvers again quickly reached the convergence criteria and showed an exactly continuous electric displacements at the boundary. Fig. 20 shows the results of both the zero charge density and constant charge density test cases. The test case shown involves

electric potentials of $-500V$ applied to the left electrode and $0V$ applied to the right electrode, a permittivity of $2\epsilon_0$ to the left and a permittivity of $0.5\epsilon_0$ to the right.

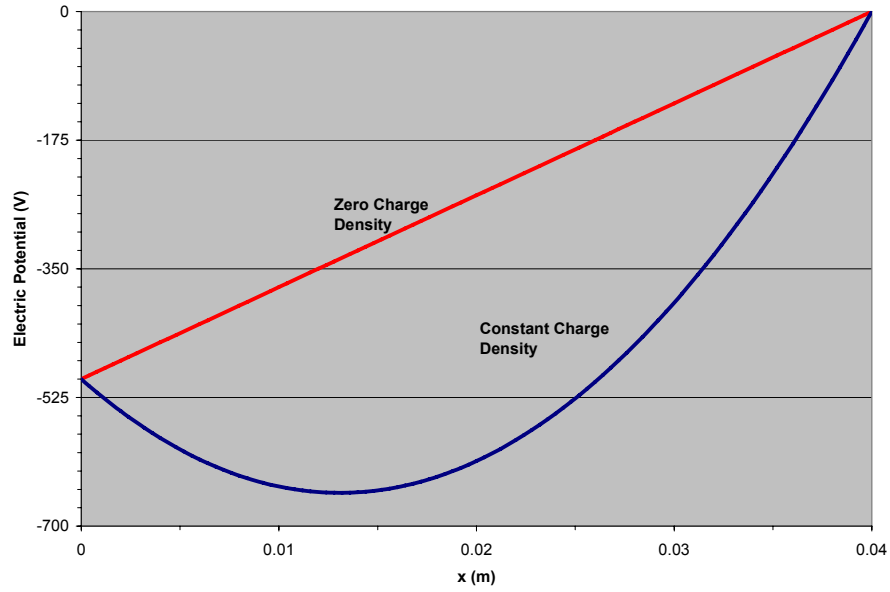


Figure 19. Poisson Check – No Dielectric

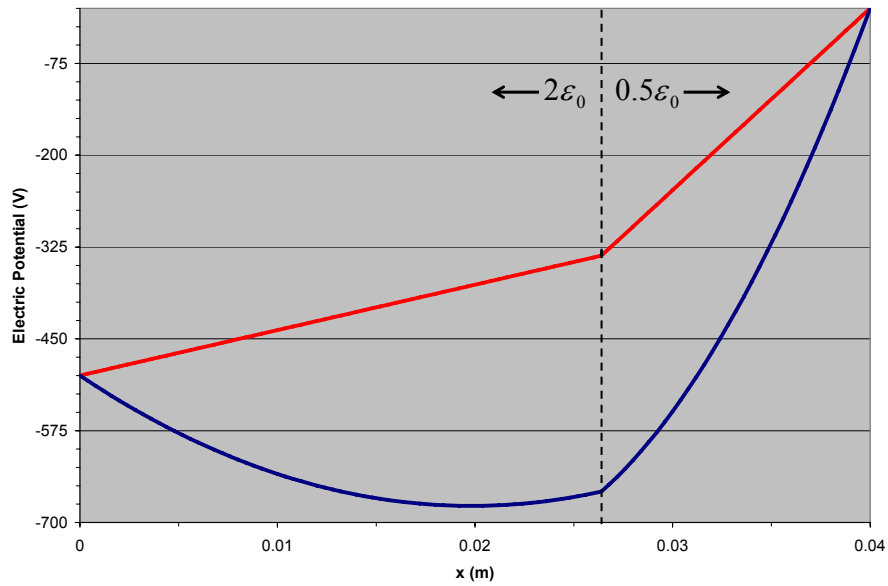


Figure 20. Poisson Check – Dielectric Inserted

With these tests completed both the fully implicit and semi-implicit Poisson solvers with and without the dielectric have been validated. This integral piece of the code can now be used in the remainder of the test cases without concern for its accuracy. This accuracy becomes extremely important for the transient sheath test case where the electric potential changes very quickly in the sheath region.

Transient Sheath

The transient sheath problem served as an excellent initial test of the semi-implicit solver two reasons. First, it creates a region with a strong electric field (sheath) that transitions into a region with little to no electric field (bulk plasma). These conditions will highlight any errors in code implementation very quickly. The second is that it is well-documented by other computational references (16:7-9; 36:4-5) so that results can easily be compared. This test excludes the electron energy equation assuming constant transport and rate coefficients.

For this test, an Argon plasma is modeled at a pressure of 100 torr. The transport and rate coefficients are

$$\begin{aligned} \mu_e &= 0.3 m^2 / V / s & \mu_p &= 10^{-3} m^2 / V / s & \nu_i &= 0.0 \\ D_e &= 0.3 m^2 / s & D_p &= 10^{-4} m^2 / s & \beta_{e-i} &= 0.0 \end{aligned} \quad (102)$$

This models a non-ionizing plasma with a characteristic electron temperature held constant at $1eV$ and an ion temperature of $0.1eV$. The recombination losses are considered to be negligible for this problem.

Initially, the left electrode is at 0V and the right side of the domain at a distance of 200 Debye lengths is free plasma. The Debye length λ_{D0} is based on conditions in the unperturbed bulk plasma and is determined by

$$\lambda_{D0} \approx 7434 \sqrt{\frac{T_e}{n_0}} \quad (103)$$

where T_e has units of eV . The electron and ion densities are equivalent and spatially uniform at $n_e = n_p = n_0 = 1.0 \times 10^{17} m^{-3}$ where n_0 is the initial charge density. Because these densities are equal and the left electrode is held at 0V, the electric potential and field are initially zero as well.

At time $t = 0s$, the potential of the left electrode is reduced to $-50V$. Formation of the sheath is initialized as electrons are repelled and ions are attracted to the negatively biased electrode. Because the electrons are much more responsive, they move quickly to the right creating a large charge discrepancy at the left boundary. As time progresses, the charges redistribute in such a way as to try to neutralize the field (16:7). Figs. 21 and 22 show the progression of the charge densities and the electric potential respectively. Note that the densities are shown in normalized form n_s / n_0 and the time progression is given in terms of $t / t_{di,p}$ where $t_{di,p}$ is the dielectric relaxation time in terms of ions only

$$t_{di,p} = \frac{\epsilon_0}{e(\mu_p n_p)} \quad (104)$$

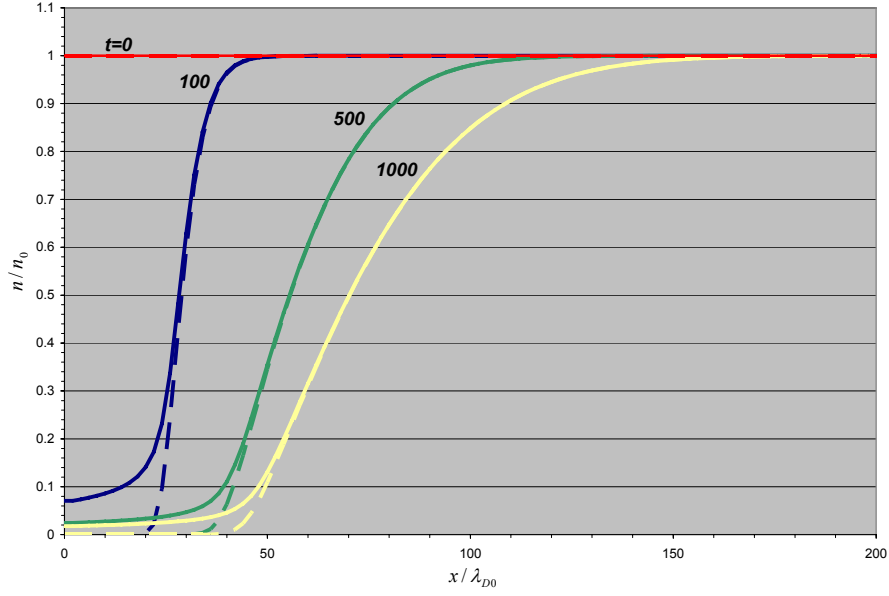


Figure 21. Transient Sheath – Sheath Progression

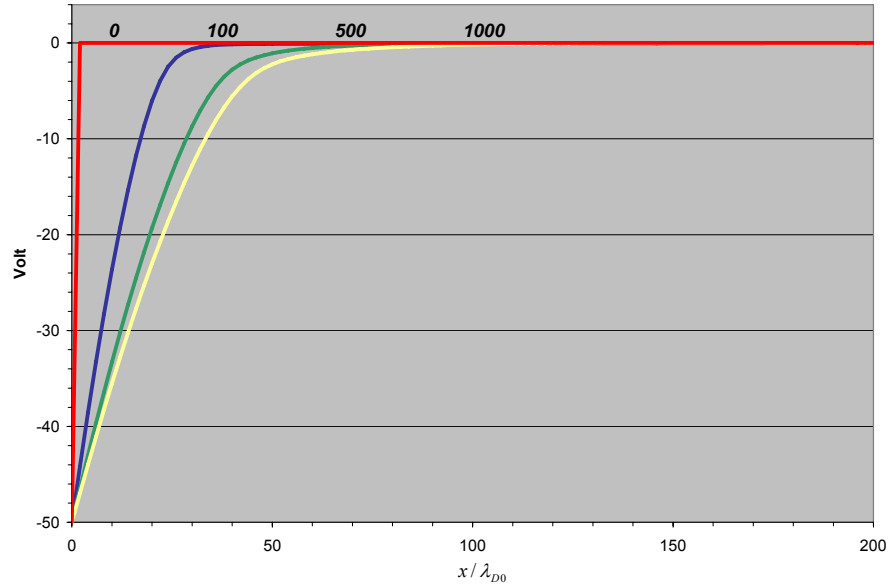


Figure 22. Transient Sheath – Electric Potential Progression

Within several tens of dual-particle dielectric relaxation times calculated by Eq. (70), electrons are lost to the bulk plasma at the right edge of the computational domain

and ions are pulled from the bulk plasma and lost to the electrode at the left. The highly mobile electrons become distributed in such a way that cancels out the field for the remainder of the bulk plasma and an electric potential such as that shown for $t/t_{di,p} = 100$ becomes the standard. The entire process continues as time advances, the sheath moves towards the bulk plasma and, as can be noted from Fig. 21, the sheath progression slows.

Qualitative comparison between the results shown in Refs. 16, 36 and Figs. 21 and 22 shows excellent agreement. This similarity demonstrates the accuracy of the semi-implicit code in modeling the sheath region of the discharge. While the transient sheath test case excludes the energy equation, it validates Poisson's equation coupled with the electron and ion continuity equations.

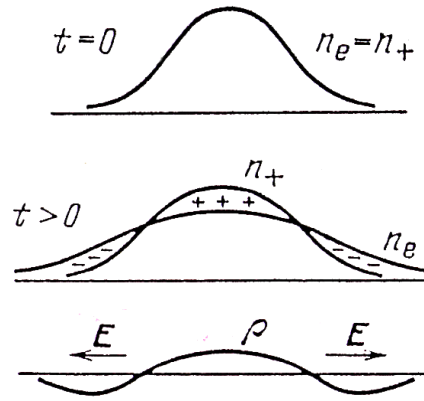


Figure 23. Ambipolar Diffusion (4:28)

Ambipolar Decay

With the transient sheath model validated, the next test case to be analyzed is ambipolar decay. Because the electrons move so much more quickly than the heavy ions, an initially quasi-neutral plasma will naturally experience a charge separation (9:28).

When there is sufficient charge density to generate a considerable space charge as they separate, a polarization field is created that opposes further separation (Fig. 23). The charges and field readjust so that the electrons are held back as the ions are pushed forward – they can only diffuse as “a team”.

It is possible to derive an analytic solution to both the particle densities and the electric field. While some of the basics will be covered here, Ref. 37 shows greater detail of the derivation (131-133). The derivation of the ambipolar electric field begins with the assumption of quasi-neutrality: $n_e \approx n_p \approx n$ and $\bar{\Gamma}_e \approx \bar{\Gamma}_p \approx \bar{\Gamma}$. These relationships yield

$$\mu_p n \bar{E} - D_i \bar{\nabla} n = \mu_e n \bar{E} - D_e \bar{\nabla} n. \quad (105)$$

Solving for the electric field gives an analytic solution of the form

$$\bar{E} = \frac{(D_p - D_e)}{(\mu_p + \mu_e)} \frac{\bar{\nabla} n}{n}. \quad (106)$$

The particle density derivation begins by substituting this electric field back into the ion flux equation yields

$$\bar{\Gamma}_p = \mu_p \frac{(D_p - D_e)}{(\mu_p + \mu_e)} \bar{\nabla} n - D_p \bar{\nabla} n = - \left(\frac{\mu_p D_e + \mu_e D_p}{\mu_p + \mu_e} \right) \bar{\nabla} n. \quad (107)$$

Solving the electron flux equation will give the same equation. The gradient multiplier becomes the ambipolar diffusion coefficient:

$$D_a = \frac{\mu_p D_e + \mu_e D_p}{\mu_p + \mu_e}. \quad (108)$$

Now the continuity equation can be written as

$$\frac{\partial n}{\partial t} + \bar{\nabla} \cdot (-D_a \bar{\nabla} n) = 0. \quad (109)$$

Because each of the coefficients on the right side of Eq. (108) is spatially uniform for this test case, D_a can be moved through the first gradient operator in Eq. (109).

Assuming that the solution to Eq. (109) can be separated as

$$n(x, t) = X(x)T(t) \quad (110)$$

then this equation can then be cast into the form

$$X \frac{dT}{dt} = D_a T \frac{d^2 X}{dx^2}. \quad (111)$$

Dividing Eq. (111) by XT , the variable separation is complete. Setting each equation equal to the constant $-1/\tau$ and solving for the time dependence yields

$$n(t) = n_0 \exp\left(\frac{-t}{\tau}\right). \quad (112)$$

The solution to the spatial equation is

$$n(x) = \sin\left(\frac{\pi}{D_a \tau}\right). \quad (113)$$

Since the density is modeled at zero at $x = 0$ and $x = L$, this means that

$$(D_a \tau)^{1/2} = \frac{L}{\pi} \quad (114)$$

or substituting $\Lambda = L / \pi$ and rearranging:

$$\tau = \frac{\Lambda^2}{D_a} \quad (115)$$

where τ becomes the characteristic time. Putting all the pieces together, the combined solution becomes

$$n(x, t) = n_0 \exp\left(-\frac{D_a}{\Lambda^2} t\right) \sin\left(\frac{\pi x}{L}\right). \quad (116)$$

For this test case, a helium plasma is modeled at 1 torr between two electrodes where each electrode is grounded. The initial density is set to $n_0 = 1 \times 10^{16} m^{-3}$. Since the solution will be in the form of a sinusoid, the charge densities are equal and initially set at

$$n_e(x) = n_p(x) = n_0 \sin\left(\frac{\pi x}{L}\right). \quad (117)$$

The transport parameters are held constant at

$$\begin{aligned} \mu_e &= 89.8 m^2 / V / s & \mu_p &= 0.8 m^2 / V / s & \nu_i &= 0.0 \\ D_e &= 101.25 m^2 / s & D_p &= (0.02 eV) \mu_p & \beta_{e-i} &= 0.0 \end{aligned} \quad (118)$$

modeling a non-ionizing helium plasma with a characteristic electron temperature of $1.1eV$ and an ion temperature at $1/40eV$. Once again, the energy continuity equation is excluded and the recombination losses considered to be negligible for this problem.

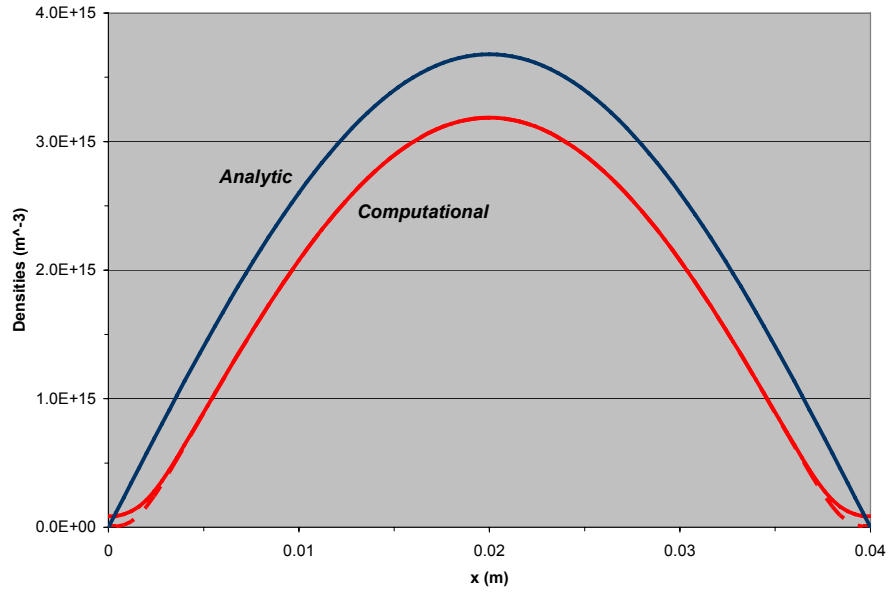


Figure 24. Ambipolar Particle Densities – Analytic and Computational

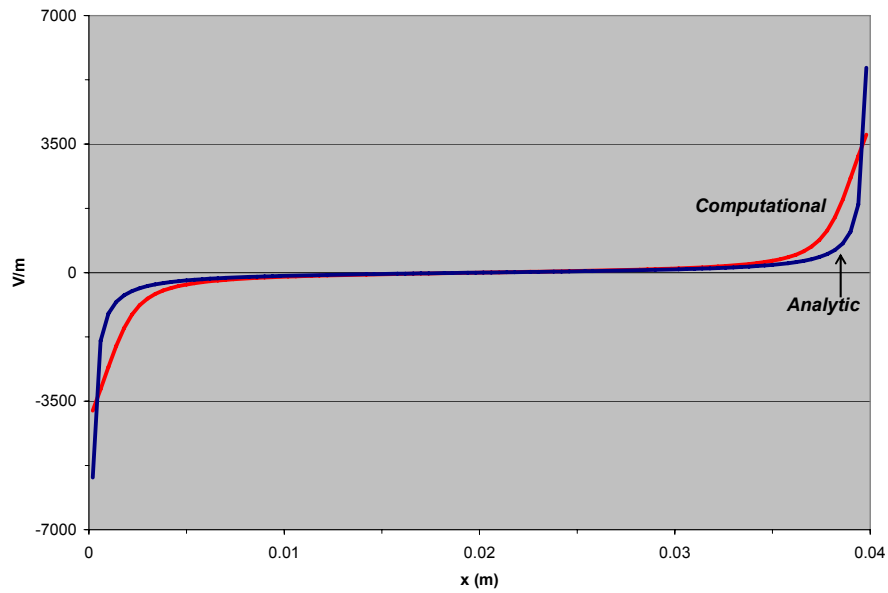


Figure 25. Ambipolar Electric Field – Analytic and Computational

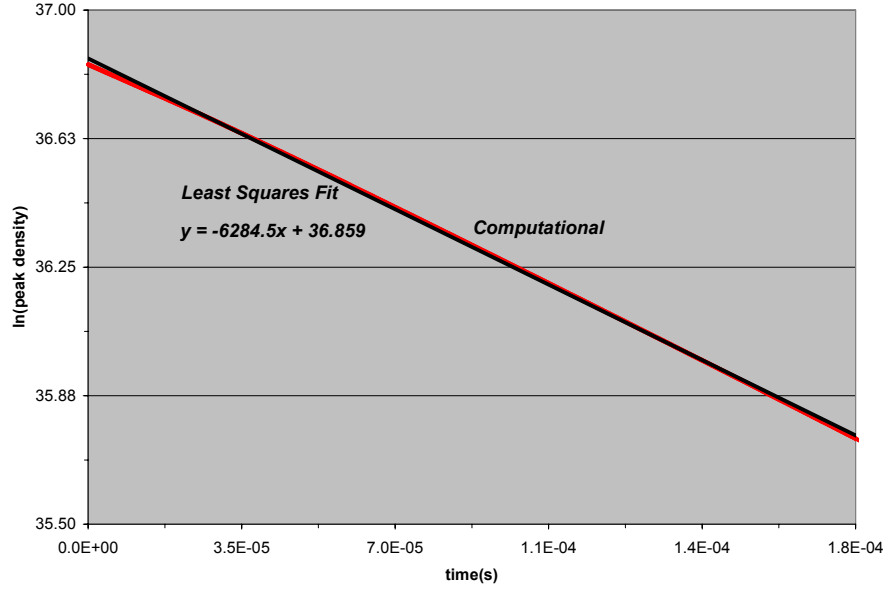


Figure 26. Natural Log of Peak Density – Ambipolar Decay

At time $t=0$, this quasi-neutral system is allowed to diffuse. Results were compared after one characteristic time interval τ . At first glance, the results did not show good agreement with the analytic solutions. As Fig. 24 shows, the particle density decays more quickly than the analytic solution predicts. Fig. 25 shows that the computational electric field does not match up near the electrode boundaries. Lastly, since the decay of the density profile is governed by the exponential in Eq. (116), the natural log of the density at one particular x -location as a function of time should be linear with a slope of $-D_a / \Lambda^2$. Fig. 26 shows the natural log of the peak density as a function of time along with the least squares linear fit. While the computational results are close to linear, there is a slight curve to the results. The slope of the least squares line is significantly more negative than the expected value of -5636.1 .

Upon further analysis, it was determined that the discrepancies came from the existence of sheath regions near both electrodes. This diagnosis came from the fact that as the initial density was increased, the slope of the natural log plot became closer to the analytic value. Increasing the initial density decreases the size of the sheath region and therefore decreased the size of the problem area.

The sheath is a problem area because as electrons and ions near the edge of the discharge, the charge density greatly diminishes and free diffusion, as opposed to ambipolar, now applies (9:28). The field created by the space charge separation is no longer large enough to keep the charged particles together and the electrons quickly leave the ions far behind. Quasi-neutrality no longer exists. Since the ambipolar analytic results depend on the maintenance of quasi-neutrality, the equations derived above do not apply in this region.

Further proof of the sheath's accelerating effect on the decay rate came with the quantification of the sheath size. The density decay rate, assumed to be a constant, is given as

$$\frac{1}{\tau} = \frac{D_a}{\Lambda^2} = \frac{D_a \pi^2}{L^2}. \quad (119)$$

This equation holds if the particle densities between $x = 0$ and $x = L$ remain quasi-neutral. As time progresses the region of quasi-neutrality decreases. Using the Debye length as the characteristic length gives the time-dependent equation for the effective Λ :

$$\Lambda(t) = \frac{L - 2\alpha \cdot \lambda_D(t)}{\pi} \quad (120)$$

where α represents the effective sheath thickness and the time-dependent Debye length relates back to the initial Debye length from Eq. (103) as

$$\lambda_D(t) = \lambda_{D0} \sqrt{\frac{n_0}{n(t)}}. \quad (121)$$

The time-dependent peak density was used as the $n(t)$ in Eq. (121). The computational decay rate was then fit using Eq. (120) in order to solve for α . A sheath thickness equal to 7.66 gave results that matched the peak density decrease with less than 1% error. Figs. 27 and 28 show these results.

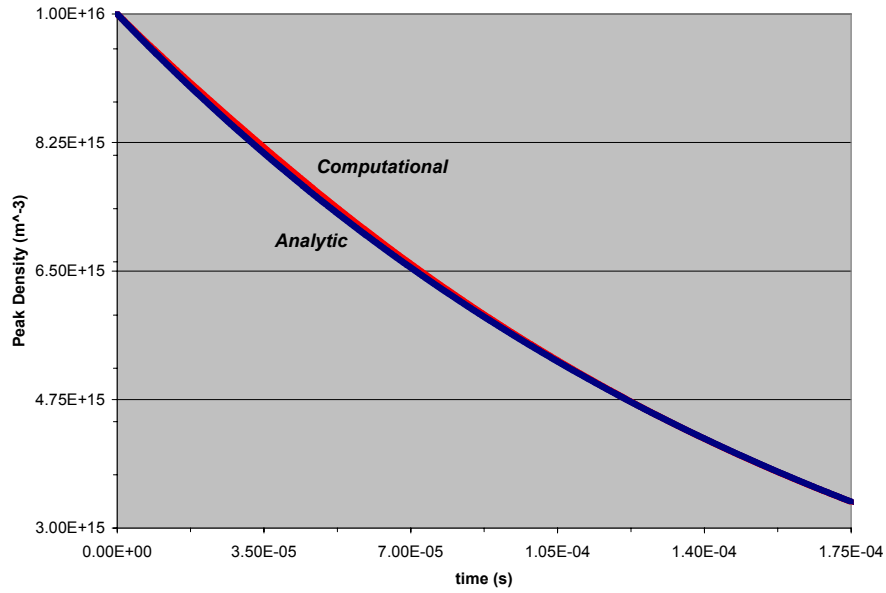


Figure 27. Time-Dependent Peak Densities

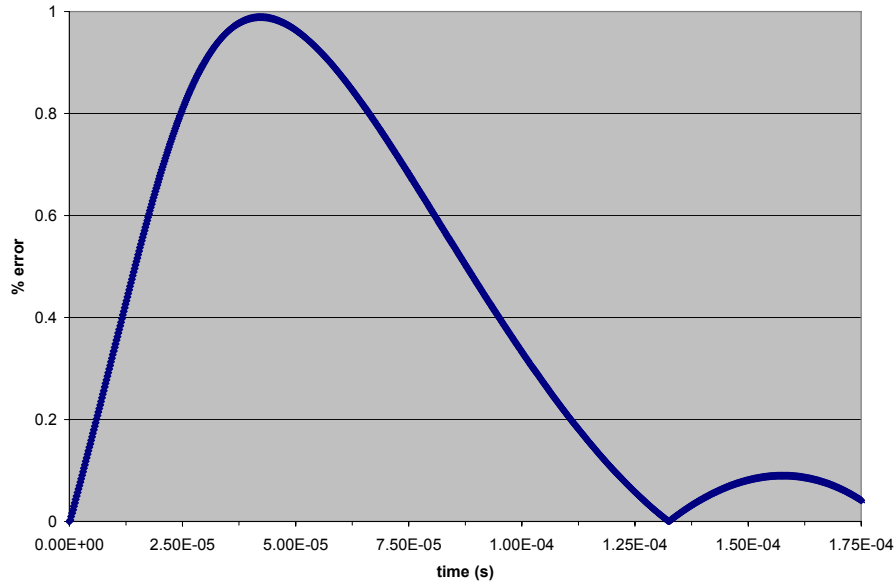


Figure 28. Percent Error for Peak Density Decay

This analysis shows excellent agreement between the computational and analytic results. The ambipolar test case was performed using both the semi-implicit and fully implicit numerical codes. While the semi-implicit results are shown above, the fully implicit showed a peak density difference of 1.85% after the characteristic time and showed excellent agreement in all regions. This test validated both codes as to the implementation of Poisson's equation coupled to the electron and ion continuity equations. Now that the first three equations in the system have been solved and validated, the energy equation will be tested.

Radio-Frequency Glow Discharge

For the final test of the semi-implicit code, a radio-frequency source was implemented along with the energy equation and source/loss terms. Similar to the transient sheath, this problem is an excellent initial test of the energy equation and

source/loss implementation for two reasons. First, the alternating sheath will be an excellent test of the code's ability to account for change in regions of strong fields. Second, this test is also well documented by other resources (16:10-12; 18; 38:2785-2786) and can therefore be qualitatively compared.

For this test case, a helium plasma is modeled at 1 torr between two electrodes separated a distance of 0.04m. The potential at the left electrode oscillates as a sinusoid with a frequency of 10 MHz and an amplitude of 500V

$$\phi_L(t) = 500 \sin(2\pi ft) \quad (122)$$

and the right electrode is grounded. The transport and source/loss coefficients are

$$\begin{aligned} \mu_e &= \mu_e[u_e] & \mu_p &= \mu_p[E/P] & \nu_i &= \nu_i[u_e] \\ D_e &= D_e[u_e] & D_p &= (0.02eV)\mu_p & \beta_{e-i} &= 1e-13m^{-3} \end{aligned} \quad (123)$$

The electron mobility and diffusion and the ion mobility coefficients are obtained by piecewise fits to the curves shown in Figs. 8, 9, 10 and 11 (Appendix C).

For this test, the initial densities were again equal and assumed to have a sinusoidal spatial distribution as shown in Eq. (117) with $n_0 = 5 \times 10^{15} m^{-3}$. At $t=0$, the AC voltage source was turned on and the discharge was allowed to run until significant changes in the peak density terminate. This takes approximately 400 cycles for this simulation. The results were recorded after the discharge had been in steady-state for more than 100 cycles. A qualitative comparison of the particle densities, electric field and current densities are then made to the results shown in Refs. 16, 18 and 38.

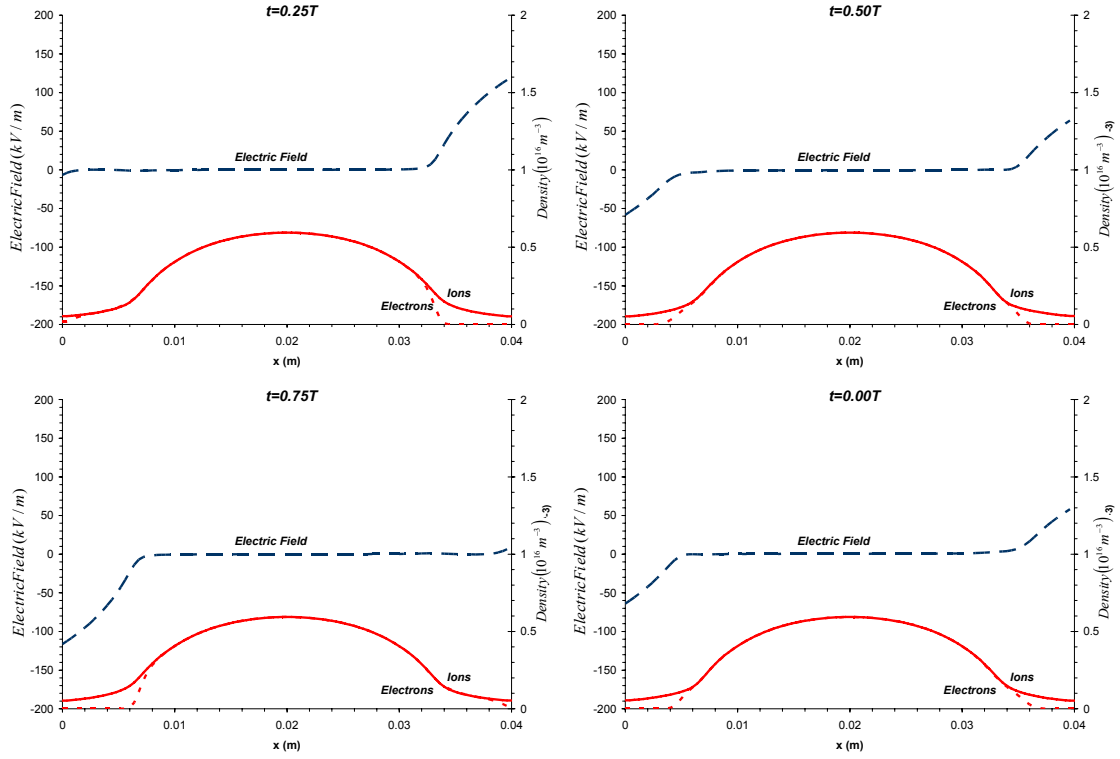


Figure 29. Semi-Implicit RF Densities and Electric Fields

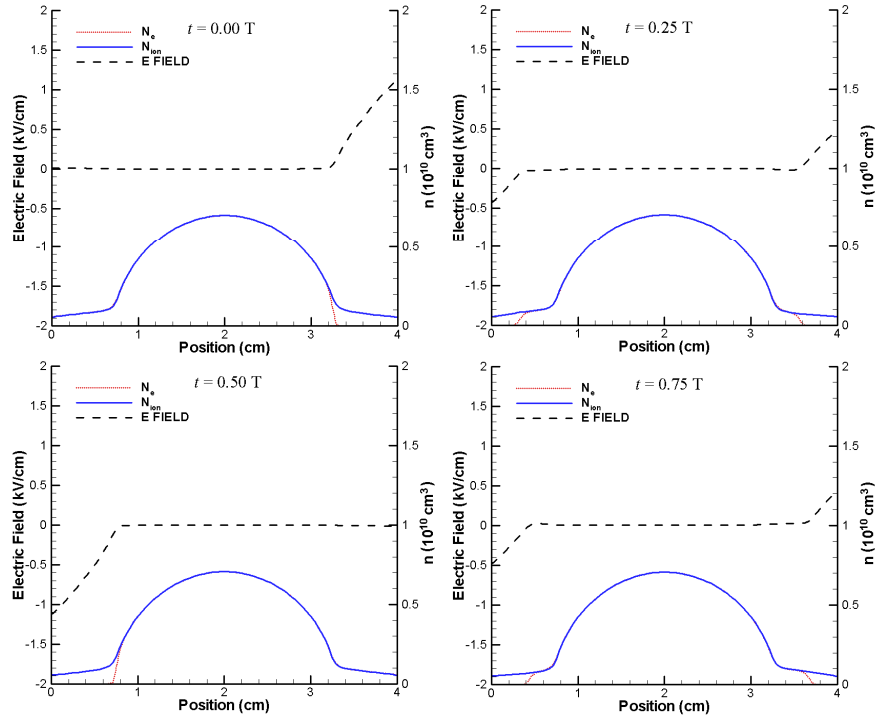


Figure 30. Results from Hilbun – RF Densities and Electric Fields (16:12)

Because the density results from each of the references are qualitatively similar, only the results from Hilbun in Ref. 16 are shown. Fig. 29 shows the computational results obtained through this numerical simulation and Fig. 30 shows the results presented by Hilbun. The result profiles show excellent agreement. Note that the results presented are a quarter cycle out of phase due to a phase shift in the driving frequency and that this code reports the values in terms of SI units whereas the Hilbun reference gives them in CGS.

For this test once in steady-state, the ion densities change very little over one voltage cycle. The mobile electrons, however, move quickly in and out of the sheath regions of the discharge. As it cycles, they are both repelled by the cycle-dependent anode and attracted to the cycle-dependent cathode. At the quarter and three-quarter cycle points, the electrons move out of the cycling cathode sheath and the positive space charge formed creates a significant electric field. At the zero and half cycle points (measured by this project) when the potential is zero on both electrodes, the electrons are evenly distributed with a small positive space charge creating a diminished electric field on each side of the discharge regime.

For the current density comparison, the electron, ion and displacement current densities were tracked over one cycle at the left (driven) electrode. These current densities are found with the equations

$$\bar{J}_{e,1/2} = q_e \cdot \left(-\frac{1}{4} n_{e,1} \bar{v}_{e,th,1/2} \right), \quad (124)$$

$$\bar{J}_{p,1/2} = q_p n_{p,1} \mu_{p,1} \bar{E}_{1/2} \quad (125)$$

and

$$\bar{J}_{d,1/2} = \epsilon_0 \frac{\partial \bar{E}_{1/2}}{\partial t} \quad (126)$$

where q is the signed electron charge. As can be seen from Fig. 31, the displacement current density at this location accounts for most of the total current density for all phases of the cycle.

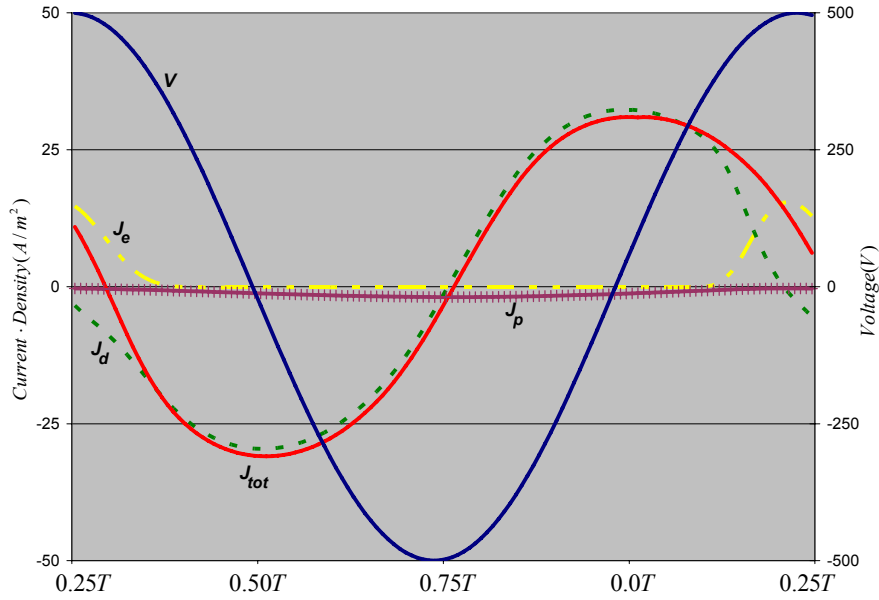


Figure 31. RF Current Densities at Left Electrode

Comparison of current densities between this project and the other references once again showed excellent agreement. There were some differences between the shapes of each individual contribution (Figs. 31 and 32). The fact that the electron flux for this code is modeled as thermal at the boundaries accounts for one of the primary

differences. The fact that the total current density must be constant and should be cyclic, phase-shifted from the voltage (38:2786) means that a change to the electron current density must change the displacement and ion current densities as well. The total current density, however, was nearly identical in both shape and magnitude for each of the comparative references.

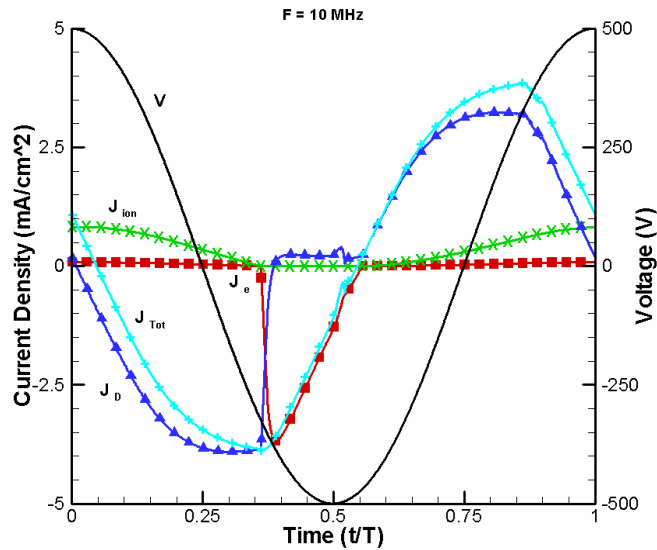


Figure 32. Results from Hilbun – RF Current Densities (16:13)

Besides small differences that could be accounted for with different or absent treatment of the energy equation as well as the thermal boundary flux conditions for electrons, this code showed excellent agreement to the references. With this test completed, the full semi-implicit model has been validated. The DBD effect on discharge current can now be accurately characterized.

The DBD Streamer

The discharge behavior changes when a dielectric barrier covers one of the electrodes. As a way to study this configuration, this project considers streamer (29:93) or streamer-regime filament (39:7569) formation in a DBD configuration. A streamer is essentially an ionization wave crossing the discharge gap. These waves will typically form when a voltage that is significantly greater than the breakdown voltage is applied to a discharge (39:7569). While much of the computational and experimental DBD studies are conducted using an AC source, this project will only address the DC simulation of this process. Because the current spike occurs so quickly in an alternating current DBD that the driving voltage changes very little during the process, a DC source is a reasonable approximation.

For this simulation, the semi-implicit code was used to model a helium plasma at 10 torr. Initially, the charged particle densities are set to a very low value ($n_0 = 5 \times 10^9 \text{ m}^{-3}$) with an ionization fraction $\sim 10^{-13}$. The initial charge density configuration resembles that of a discharge with a cathode sheath already formed (Fig. 34a). Because the assumed low value of the initial charge densities, the electric field is essentially constant throughout the computational domain at the initiation of the simulation. The transport and rate coefficients used are the same as those for the RF test case given in Eq. (123).

An additional loss term is added to the system of equations in order to better model an actual discharge. This term considers a diffusion loss to the walls of the discharge tube. This radial diffusion is considered to be ambipolar and the loss is taken as

$$L_{Da} = -\frac{D_a}{\Lambda^2} n_s \quad (127)$$

where the ‘s’ makes the loss specific to the density of each particle type. Even though this loss is modeled as ambipolar, the charged particle densities will be different in certain regions of the discharge and this general equation takes that into account. Since this model only considers radial losses, $\Lambda = R/2.4$ (9:67) where R represents the radius of the discharge tube at 0.02m.

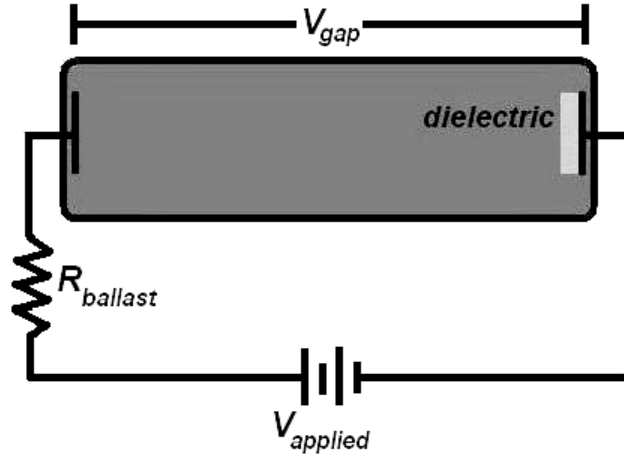


Figure 33. Dielectric Circuit Configuration for Streamer Simulation

For the voltage configuration of this test case, a circuit is constructed to resemble that shown in Fig.. The applied system voltage is -2.5kV and the ballast resistance is set to 12.5kΩ. The effective capacitance of the dielectric barrier is assumed to have a negligible effect on the circuit behavior and is therefore ignored. The effect of the dielectric barrier is modeled as described by Eq. (58).

The potential applied to the left electrode becomes

$$V_{gap} = V_{applied} - IR_{ballast} \quad (128)$$

where I represents the current determined by

$$I = (\bar{J}_e + \bar{J}_p)A. \quad (129)$$

A is the area of the left electrode assumed to be $(0.05)^2 \pi$. The current densities are determined by Eqs. (124) and (125) and is calculated at $x = 0.02m$. The displacement current is excluded because of difficulties incorporating this contribution into the feedback system implemented for this simulation and is recognized to be a source of some error in the results presented. The general features of the discharge evolution, however, are consistent with experimental observations and earlier simulations in a bare electrode configuration (16:15-18). The right electrode is grounded.

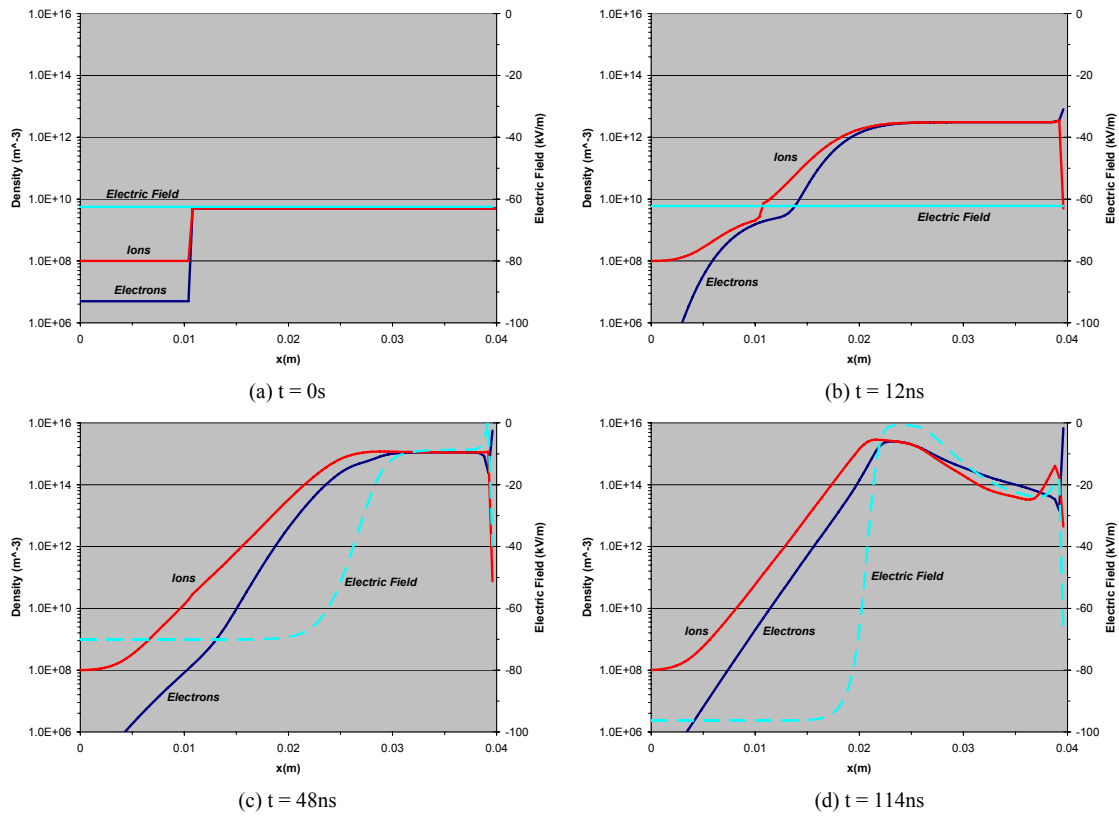


Figure 34. DBD Streamer Evolution – (a) Initial distribution (b) Homogenous avalanche (c) Space-charge dominated avalanche (d) Cathode-directed streamer

The results of this simulation show the evolution of the streamer and the effect of the dielectric barrier on this evolution (Fig. 34a-d) . Because the simulation begins with a plateau of charge across the right side of the domain, the density growth and sheath progression to the right represent the electron avalanche associated with breakdown in the gap (Fig. 34b). The wave of ionization is directed toward the anode (buried electrode) in this phase. As the electrons are driven to the right by the negative (left-directed) electric field, the ionization cascade creates a trail of ions that can not quite keep up with the electron progression. This phase of the discharge cycle is called the homogenous avalanche (16:17) because the density growth is governed by the electron advance in a nearly uniform electric field.

The next phase in the streamer evolution occurs as the charge densities and space charge separation become significant enough to alter the electric field (Fig. 34c). The charges redistribute themselves so as to reduce the electric field in the avalanche (maximum charge) region of the discharge. As these charges diminish the electric field within the avalanche, the field to the left and at the dielectric becomes even stronger. During this phase, a shift in the ionization occurs. Originally, the greatest ionization occurred within the avalanche as it progressed from the cathode to the anode. Now, more ionization occurs to the left of the avalanche where the field has increased than in the avalanche itself where the field has weakened. This is the space-charge dominated avalanche phase (16:17).

The final phase is associated with a change in the direction of the wave now streaming towards the cathode (Fig. 34d). As the field strength to the left of the avalanche continues to grow, the ionization in this region remains significant. Because the field is still negative, it pulls the new ions to the left as it pushes the new electrons to the right. Accordingly, this new ionization wave, labeled the cathode-directed streamer (16:17), has a net positive charge at the streamer head. This positive space charge acts as an effective anode and as the streamer continues to approach the cathode, the electric field becomes increasingly negative in the interim region.

During the first two phases of the discharge (Fig. 34b and 34c), the avalanche progression is very similar to that of a non-barrier microdischarge (16:16). The surface charge on the dielectric increases during the avalanche, however, and alters the discharge behavior for the final phase of the DBD. During this phase, the charge accumulation plays an important role.

As the ionization wave from an anode-directed avalanche transitions to a cathode-directed streamer, the negative surface charge that has accumulated on the dielectric reaches a saturation value. This surface charge is shown in Fig. (34) as the right-most point in each of the density plots and should be distinguished from the volume charge density shown for the remainder of the domain. The particles between the dielectric surface and the streamer head begin to redistribute such that the space charge diminishes and the field in this region continues to diminish as well.

This field reduction becomes important when considering the discharge circuit described by Eq. (128). As the avalanche progresses to the right, the current flowing to the left electrode diminishes the gap potential. As the charge density grows increasingly

negative on the dielectric surface, the gap potential is reduced even further. A sharp rise in the current associated with the cathode-directed streamer again reduces the gap potential. This reduction in the gap potential will progress due to the accumulation of surface charge until the voltage falls below the self-maintenance value and the discharge will eventually extinguish. In this relatively low pressure discharge where recombination is not as large, this progression may include a temporary transition to a glow discharge before this charge build-up on the dielectric becomes significant enough to extinguish the discharge.

The importance of streamer or filament formation in the DBD becomes evident when comparing the right-ward and left-ward movement of the charged particles. Because the streamer carries both ions and electrons in its ionization wave, the asymmetry associated with the streamer is a very interesting characteristic. There are a significantly larger number of ions involved with the cathode-directed streamer than there are in the anode-directed avalanche. If it is assumed that ion-neutral collisions dominate the momentum transfer to the flow (16:18) then a source of the observed asymmetry in flow control could be explained, at least in part, by streamer propagation.

The true determination of the source of the added flow momentum has yet to be definitively determined. There is a great deal more research that remains to be done on this subject. Additionally, there are several model assumptions made in this project that deserve more investigation. Each of these subjects will be covered in the final chapter.

V. DBD Modeling – Accomplishments and the Next Round

This numerical study examined plasma dynamics in a dielectric-barrier discharge configuration. While this investigation took one small step towards a better understanding of DBD operation, there still remains a great deal more to be studied and characterized. Some of the lessons learned as well as ideas for continuing investigation will be discussed.

Looking Back

This research achieved far more than a simple DBD streamer characterization. The intermediate results of this research were validated against previously published computational models. An accurate one-dimensional code was implemented, tested and validated. An alternative numerical approach was also implemented and partially validated. This fully implicit method improved upon the semi-implicit formalism with an increased time step and the promise of increased accuracy. The validation procedure and observed consistency of the two numerical approaches ensured that the DBD simulation yielded accurate numerical results. This simulation extended current numerical work in characterizing the streamer cycle when a dielectric barrier blocks one electrode.

Accurate 1-D Model

Before the computational models could be used to investigate DBD characteristics, they first had to be validated. While there is much documentation as to the numerical intricacies involved in developing a plasma discharge model, this specific implementation had to be rigorously tested and the results compared to either previously

validated results or analytic solutions. The full implementation of the semi-implicit code was tested and validated through the analytic Poisson, transient sheath, ambipolar decay and RF simulations.

The Poisson check showed excellent agreement with the analytic results and demonstrated that the solution to Poisson's equation was accurate for both the semi-implicit and fully implicit models. The transient sheath test case agreed with two previously validated models and showed that the coupling between the electron/ion continuity equations and Poisson's had been correctly implemented. It also established that the semi-implicit code yielded an accurate model of the discharge sheath. The ambipolar test case showed excellent agreement with the analytic solutions for the electric field and charge density profile once the sheath region was taken into account. The sheath analysis showed agreement to within 1% relative error for every time step of the decay and validated the implementation of the ion/electron continuity equations coupled with Poisson's for both the semi-implicit and fully implicit models.

Fully Implicit Advantages

Although there was not enough time to completely implement and test the fully implicit code, the benefits of this solution technique became obvious in the ambipolar diffusion test. Because there is no lag between Poisson's solution and the particle/energy continuity calculations, a larger time step can be taken. For the ambipolar test case, this time step was three to four orders of magnitude greater than that of the semi-implicit method. Additionally, the total execution time was reduced by a factor of four.

DBD Streamer Characterization

The final phase to this project simulated the streamer formation during a DBD discharge initiation. This characterization detailed three different phases of the DBD cycle. The first two phases of the DBD were the anode-directed homogenous avalanche and space-charge dominated avalanche. The third phase was the cathode-directed streamer. This simulation confirmed the asymmetry between the anode-directed avalanche and the cathode-directed streamer. A comparison to experimental and non-barrier computational results showed general agreement.

Looking Forward

Fully Implicit Development

Due to time constraints, a full implementation for the simultaneous solution could not be accomplished. Implementation of the energy equation was problematic. In regions where the electric field was strong and the electron densities were small, negative energies were encountered in the Newton-Raphson iteration process. Additionally, once the energy equation was implemented, the time steps required to maintain stability dropped below those used for the semi-implicit solution.

Boeuf introduces a time-dependent Poisson's equation in Ref. 25. In that particular study, the equation is used in a semi-implicit numerical formalism. However, Boeuf reports that this implementation added enough stability to the method that time steps as large as fifty times the dielectric relaxation time could be taken. This added stability would certainly transfer to the fully implicit model as well.

Mean Velocity Flux

Hammond proposes a novel discretization technique in his paper addressing RF plasma discharge simulations (Ref. 40). This mean velocity flux discretization is a method that could be employed to replace the Scharfetter-Gummel discretization. This method promises increased accuracy of the solution and a decrease in the computational cost of the flux calculations. This method of flux discretization certainly deserves more exploration.

Continued Dielectric Studies

There still remain a large number of topics to be considered pertaining to the dielectric barrier discharge. Studies involving AC voltage sources, differing dielectric/charge-interaction models as well as moving to two or three dimensions and various electrode configurations name just a few of the possibilities. Something that becomes increasingly important as the investigation moves to multiple dimensions is the Poisson solver. If the asymmetric electrode configuration shown in Fig. 7 is modeled, the boundary conditions for Poisson's equation get far more complicated.

In order to pin-point the source of the observed flow control, many of the subjects listed above will need to be addressed. The future goal for the continuation of this project is to create a computational tool that can be used to simulate a plasma discharge in all configurations. This tool would include the ability to add the dielectric barrier to any number of electrodes, model in one or two dimensions with a variety of electrode geometries. This tool could be used to study the effects of the barrier on the discharges. In the process, it could possibly pinpoint the mechanism that drives DBD flow control.

Depending upon what this mechanism is, the possibilities for actuator technologies could be endless.

Appendix A. Model Assumptions

Many of the model assumptions match those of Boeuf and Pitchford (14:1377). The general model assumptions for this project are:

- Neglect interactions between the charged particles and neutral atoms in excited states
- Only electron ionization from the ground state is considered
- Electron-electron collisions are not taken into account
- Ion inertia is neglected
- Ion distribution is assumed Maxwellian
- Electron inertia and energy gradient terms are neglected in the electron momentum equation
- Pressure tensor is assumed isotropic and diagonal
- Electron drift energy is considered negligible with respect to the electron thermal energy
- Heat flux is proportional to the electron temperature gradient
- Mean electron-neutral collision rates are proportional only to the electron mean energy
- The electron diffusion term is essentially constant over small spatial regions and can be pulled through the gradient operator as a constant for the drift portion of the energy density flux equation

Appendix B. Newton-Raphson Matrix

Original PHI equation:

$$PHI[\varphi, ne, np] = \left(\frac{(\varphi_{i+1}^{k+1,m+1}) - 2(\varphi_i^{k+1,m+1}) + (\varphi_{i-1}^{k+1,m+1})}{(\Delta x)^2} \right) + \frac{q}{\varepsilon_0} (n_{p,i}^{k+1,m+1} - n_{e,i}^{k+1,m+1}) = 0 \quad (130)$$

Newton-Raphson equation:

$$\begin{aligned} PHI[\varphi, ne, np] = & \left(\frac{1}{(\Delta x)^2} \right) \delta \varphi_{i-1}^{k,m+1} \\ & + \left(\frac{-2}{(\Delta x)^2} \right) \delta \varphi_i^{k,m+1} - \frac{q}{\varepsilon_0} \delta n_{e,i}^{k,m+1} + \frac{q}{\varepsilon_0} \delta n_{p,i}^{k,m+1} \\ & + \left(\frac{1}{(\Delta x)^2} \right) \delta \varphi_{i+1}^{k,m+1} \\ & + \left(\frac{(\varphi_{i+1}^{k,m+1}) - 2(\varphi_i^{k,m+1}) + (\varphi_{i-1}^{k,m+1})}{(\Delta x)^2} \right) + \frac{q}{\varepsilon_0} (n_{p,i}^{k,m+1} - n_{e,i}^{k,m+1}) = 0 \end{aligned} \quad (131)$$

Original NP equation:

$$NP[\varphi, n_e, n_p, (n_e u_e)] = \frac{n_{p,i}^{k+1,m+1} - n_{p,i}^{k,m}}{\Delta t} + \frac{1}{2} \left(\frac{\Gamma_{p,i+1/2}^{k+1,m+1} - \Gamma_{p,i-1/2}^{k+1,m+1}}{\Delta x} + \frac{\Gamma_{p,i+1/2}^{k,m} - \Gamma_{p,i-1/2}^{k,m}}{\Delta x} \right) - \Delta t \nu \left[\frac{(n_e u_e)_i^{k+1,m+1}}{n_{e,i}^{k+1,m+1}} \right] * n_{e,i}^{k,m+1} = 0 \quad (132)$$

Newton-Raphson equation:

$$\begin{aligned} NP[\varphi, n_e, n_p, (n_e u_e)] = & -\frac{\Delta t}{2\Delta x} \left(\frac{\partial \Gamma_{p,i-1/2}^{k,m+1}}{\partial \varphi_{i-1}} \right) \delta \varphi_{i-1}^{k,m+1} - \frac{\Delta t}{2\Delta x} \left(\frac{\partial \Gamma_{p,i-1/2}^{k,m+1}}{\partial n_{p,i-1}} \right) \delta n_{p,i-1}^{k,m+1} \\ & + \frac{\Delta t}{2\Delta x} \left(\left(\frac{\partial \Gamma_{p,i+1/2}^{k,m+1}}{\partial \varphi_i} \right) - \left(\frac{\partial \Gamma_{p,i-1/2}^{k,m+1}}{\partial \varphi_i} \right) \right) \delta \varphi_i^{k,m+1} - \Delta t \left(\frac{\partial \nu_i^{k,m+1}}{\partial \langle u_e \rangle_i^{k,m+1}} \right) \left(\frac{-(n_e u_e)_i^{k,m+1}}{(n_{e,i}^{k,m+1})^2} \right) \cdot n_{e,i}^{k,m+1} \delta n_{e,i}^{k,m+1} \\ & + \left(1 + \frac{\Delta t}{2\Delta x} \left(\frac{\partial \Gamma_{p,i+1/2}^{k,m+1}}{\partial n_{p,i}} \right) - \frac{\Delta t}{2\Delta x} \left(\frac{\partial \Gamma_{p,i-1/2}^{k,m+1}}{\partial n_{p,i}} \right) \right) \delta n_{p,i}^{k,m+1} \\ & - \Delta t \left(\frac{\partial \nu_i^{k,m+1}}{\partial \langle u_e \rangle_i^{k,m+1}} \right) \left(\frac{1}{n_{e,i}^{k,m+1}} \right) (n_{e,i}^{k,m+1}) \delta (n_e u_e)_i^{k,m+1} \\ & + \frac{\Delta t}{2\Delta x} \left(\frac{\partial \Gamma_{p,i+1/2}^{k,m+1}}{\partial \varphi_{i+1}} \right) \delta \varphi_{i+1}^{k,m+1} + \frac{\Delta t}{2\Delta x} \left(\frac{\partial \Gamma_{p,i+1/2}^{k,m+1}}{\partial n_{p,i+1}} \right) \delta n_{p,i+1}^{k,m+1} \\ & + \frac{\Delta t}{2\Delta x} \left((\Gamma_{p,i+1/2}^{k,m+1} - \Gamma_{p,i-1/2}^{k,m+1}) + (\Gamma_{p,i+1/2}^{k,m} - \Gamma_{p,i-1/2}^{k,m}) \right) - \\ & \Delta t \left(\nu \left[\frac{(n_e u_e)_i^{k,m+1}}{n_{e,i}^{k,m+1}} \right] \right) n_{e,i}^{k,m+1} + n_{p,i}^{k,m+1} - n_{p,i}^{k,m} = 0 \end{aligned} \quad (133)$$

Original EN equation (not yet validated):

$$\begin{aligned}
EN[\varphi, n_e, (n_e u_e)] &= (n_e u_e)_i^{k,m+1} + \delta(n_e u_e)_i^{k,m+1} - (n_e u_e)_i^{k,m} + \\
&\frac{5}{3} * \frac{\Delta t}{2\Delta x} \left((\Gamma_{\varepsilon,i+1/2}^{k,m+1} + \delta\Gamma_{\varepsilon,i+1/2}^{k,m+1}) - (\Gamma_{\varepsilon,i-1/2}^{k,m+1} + \delta\Gamma_{\varepsilon,i-1/2}^{k,m+1}) + (\Gamma_{\varepsilon,i+1/2}^{k,m} - \Gamma_{\varepsilon,i-1/2}^{k,m}) \right) \\
&- \frac{\Delta t}{4\Delta x} (\Gamma_{e,i+1/2}^{k,m+1} + \Gamma_{e,i-1/2}^{k,m+1}) * (\varphi_{i+1}^{k,m+1} - \varphi_{i-1}^{k,m+1}) \\
&+ \Delta t \left(k_L \left[\frac{(n_e u_e)_i^{k,m+1}}{n_{e,i}^{k,m+1}} \right] + \delta k_L \left[\frac{(n_e u_e)_i^{k,m+1}}{n_{e,i}^{k,m+1}} \right] \right) \cdot n_{e,i}^{k,m+1} N = 0
\end{aligned} \tag{134}$$

Newton-Raphson equation:

$$\begin{aligned}
EN[\varphi, ne, (n_e u_e)] &= -\frac{5\Delta t}{6\Delta x} \left(\frac{\partial \Gamma_{\varepsilon,i-1/2}^{k,m+1}}{\partial \varphi_{i-1}} \right) \delta \varphi_{i-1}^{k,m+1} - \frac{5\Delta t}{6\Delta x} \left(\frac{\partial \Gamma_{\varepsilon,i-1/2}^{k,m+1}}{\partial (n_e u_e)_{i-1}} \right) \delta (n_e u_e)_{i-1} \\
&+ \frac{5\Delta t}{6\Delta x} \left(\left(\frac{\partial \Gamma_{\varepsilon,i+1/2}^{k,m+1}}{\partial \varphi_i} \right) - \left(\frac{\partial \Gamma_{\varepsilon,i-1/2}^{k,m+1}}{\partial \varphi_i} \right) \right) \delta \varphi_i^{k,m+1} \\
&+ \Delta t \left(\frac{\partial k_{Li}^{k,m+1}}{\partial u_{e,i}^{k,m+1}} \right) \left(\frac{-(n_e u_e)_i^{k,m+1}}{(n_{e,i}^{k,m+1})^2} \right) \cdot n_{e,i}^{k,m+1} N \cdot \delta n_{e,i}^{k,m+1} \\
&+ \left(1 + \frac{5\Delta t}{6\Delta x} \left(\left(\frac{\partial \Gamma_{\varepsilon,i+1/2}^{k,m+1}}{\partial (n_e u_e)_i} \right) - \left(\frac{\partial \Gamma_{\varepsilon,i-1/2}^{k,m+1}}{\partial (n_e u_e)_i} \right) \right) \right. \\
&\quad \left. + \Delta t \left(\frac{\partial k_{Li}^{k,m+1}}{\partial u_{e,i}^{k,m+1}} \right) \left(\frac{\partial \varepsilon_i^{k,m+1}}{\partial (n_e u_e)_i^{k,m+1}} \right) * n_{e,i}^{k,m+1} * N \right) \delta (n_e u_e)_i^{k,m+1} \\
&+ \frac{5\Delta t}{6\Delta x} \left(\frac{\partial \Gamma_{\varepsilon,i+1/2}^{k,m+1}}{\partial \varphi_{i+1}} \right) \delta \varphi_{i+1}^{k,m+1} + \frac{5\Delta t}{6\Delta x} \left(\frac{\partial \Gamma_{\varepsilon,i+1/2}^{k,m+1}}{\partial (n_e u_e)_{i+1}} \right) \delta (n_e u_e)_{i+1}^{k,m+1} \\
&(n_e u_e)_i^{k,m+1} - (n_e u_e)_i^{k,m} + \frac{5\Delta t}{6\Delta x} \left((\Gamma_{\varepsilon,i+1/2}^{k,m+1} - \Gamma_{\varepsilon,i-1/2}^{k,m+1}) + (\Gamma_{\varepsilon,i+1/2}^{k,m} - \Gamma_{\varepsilon,i-1/2}^{k,m}) \right) \\
&- \frac{\Delta t}{4\Delta x} (\Gamma_{e,i+1/2}^{k,m+1} + \Gamma_{e,i-1/2}^{k,m+1}) * (\varphi_{i+1}^{k,m+1} - \varphi_{i-1}^{k,m+1}) \\
&+ \Delta t \left(k_L \left[\frac{(n_e u_e)_i^{k,m+1}}{n_{e,i}^{k,m+1}} \right] \right) * n_{e,i}^{k,m+1} N = 0
\end{aligned} \tag{135}$$

Coefficients for A_i - first index is row, second index is column (all fourth columns are not yet validated):

$$\begin{aligned}
A_{11} &= \left(\frac{-2}{(\Delta x)^2} \right) & A_{12} &= -\frac{q \cdot n_0}{\varepsilon_0} & A_{13} &= \frac{q \cdot n_0}{\varepsilon_0} & A_{14} &= 0 \\
A_{21} &= \frac{\Delta t}{2\Delta x} \left(\left(\frac{\partial \Gamma_{e,i+1/2}^{k,m+1}}{\partial \varphi_i} \right) - \left(\frac{\partial \Gamma_{e,i-1/2}^{k,m+1}}{\partial \varphi_i} \right) \right) & A_{22} &= \begin{pmatrix} 1 + \frac{\Delta t}{2\Delta x} \left(\frac{\partial \Gamma_{e,i+1/2}^{k,m+1}}{\partial n_{e,i}} \right) - \frac{\Delta t}{2\Delta x} \left(\frac{\partial \Gamma_{e,i-1/2}^{k,m+1}}{\partial n_{e,i}} \right) \\ -\Delta t \left(\frac{\partial v_i^{k,m+1}}{\partial \langle u_e \rangle_i^{k,m+1}} \right) \left(\frac{-(n_e u_e)_i^{k,m+1}}{(n_{e,i}^{k,m+1})^2} \right) \cdot n_{e,i}^{k,m+1} \end{pmatrix} \\
A_{23} &= 0 & A_{24} &= -\Delta t \left(\frac{\partial v_i^{k,m+1}}{\partial \langle u_e \rangle_i^{k,m+1}} \right) \left(\frac{1}{n_{e,i}^{k,m+1}} \right) (n_{e,i}^{k,m+1}) \\
A_{31} &= \frac{\Delta t}{2\Delta x} \left(\left(\frac{\partial \Gamma_{p,i+1/2}^{k,m+1}}{\partial \varphi_i} \right) - \left(\frac{\partial \Gamma_{p,i-1/2}^{k,m+1}}{\partial \varphi_i} \right) \right) & A_{32} &= -\Delta t \left(\frac{\partial v_i^{k,m+1}}{\partial \langle u_e \rangle_i^{k,m+1}} \right) \left(\frac{-(n_e u_e)_i^{k,m+1}}{(n_{e,i}^{k,m+1})^2} \right) \cdot n_{e,i}^{k,m+1} \\
A_{33} &= \left(1 + \frac{\Delta t}{2\Delta x} \left(\frac{\partial \Gamma_{p,i+1/2}^{k,m+1}}{\partial n_{p,i}} \right) - \frac{\Delta t}{2\Delta x} \left(\frac{\partial \Gamma_{p,i-1/2}^{k,m+1}}{\partial n_{p,i}} \right) \right) & A_{34} &= -\Delta t \left(\frac{\partial v_i^{k,m+1}}{\partial \langle u_e \rangle_i^{k,m+1}} \right) \left(\frac{1}{n_{e,i}^{k,m+1}} \right) (n_{e,i}^{k,m+1}) \\
A_{41} &= \frac{5\Delta t}{6\Delta x} \left(\left(\frac{\partial \Gamma_{\varepsilon,i+1/2}^{k,m+1}}{\partial \varphi_i} \right) - \left(\frac{\partial \Gamma_{\varepsilon,i-1/2}^{k,m+1}}{\partial \varphi_i} \right) \right) & A_{42} &= \Delta t \left(\frac{\partial k_{Li}^{k,m+1}}{\partial u_{e,i}^{k,m+1}} \right) \left(\frac{-(n_e u_e)_i^{k,m+1}}{(n_{e,i}^{k,m+1})^2} \right) \cdot n_{e,i}^{k,m+1} N \\
A_{43} &= 0 & A_{44} &= \begin{pmatrix} 1 + \frac{5\Delta t}{6\Delta x} \left(\left(\frac{\partial \Gamma_{\varepsilon,i+1/2}^{k,m+1}}{\partial (n_e u_e)_i} \right) - \left(\frac{\partial \Gamma_{\varepsilon,i-1/2}^{k,m+1}}{\partial (n_e u_e)_i} \right) \right) \\ + \Delta t \left(\frac{\partial k_{Li}^{k,m+1}}{\partial u_{e,i}^{k,m+1}} \right) \left(\frac{\partial \varepsilon_i^{k,m+1}}{\partial (n_e u_e)_i^{k,m+1}} \right) * n_{e,i}^{k,m+1} * N \end{pmatrix}
\end{aligned}$$

Coefficients for B_i :

$$\begin{aligned}
B_{11} &= \left(\frac{1}{(\Delta x)^2} \right) & B_{12} &= 0 & B_{13} &= 0 & B_{14} &= 0 \\
B_{21} &= \frac{\Delta t}{2\Delta x} \left(\frac{\partial \Gamma_{e,i+1/2}^{k,m+1}}{\partial \varphi_{i+1}} \right) & B_{22} &= \frac{\Delta t}{2\Delta x} \left(\frac{\partial \Gamma_{e,i+1/2}^{k,m+1}}{\partial n_{e,i+1}} \right) & B_{23} &= 0 & B_{24} &= 0
\end{aligned}$$

$$B_{31} = \frac{\Delta t}{2\Delta x} \left(\frac{\partial \Gamma_{p,i+1/2}^{k,m+1}}{\partial \varphi_{i+1}} \right) \quad B_{32} = 0 \quad B_{33} = \frac{\Delta t}{2\Delta x} \left(\frac{\partial \Gamma_{p,i+1/2}^{k,m+1}}{\partial n_{p,i+1}} \right) \quad B_{34} = 0$$

$$B_{41} = \frac{5\Delta t}{6\Delta x} \left(\frac{\partial \Gamma_{\varepsilon,i+1/2}^{k,m+1}}{\partial \varphi_{i+1}} \right) \quad B_{42} = 0 \quad B_{43} = 0 \quad B_{44} = \frac{5\Delta t}{6\Delta x} \left(\frac{\partial \Gamma_{\varepsilon,i+1/2}^{k,m+1}}{\partial (n_e u_e)_{i+1}} \right)$$

Coefficients for C_i :

$$C_{11} = \left(\frac{1}{(\Delta x)^2} \right) \quad C_{12} = 0 \quad C_{13} = 0 \quad C_{14} = 0$$

$$C_{21} = -\frac{\Delta t}{2\Delta x} \left(\frac{\partial \Gamma_{e,i-1/2}^{k,m+1}}{\partial \varphi_{i-1}} \right) \quad C_{22} = -\frac{\Delta t}{2\Delta x} \left(\frac{\partial \Gamma_{e,i-1/2}^{k,m+1}}{\partial n_{e,i-1}} \right) \quad C_{23} = 0 \quad C_{24} = 0$$

$$C_{31} = -\frac{\Delta t}{2\Delta x} \left(\frac{\partial \Gamma_{p,i-1/2}^{k,m+1}}{\partial \varphi_{i-1}} \right) \quad C_{32} = 0 \quad C_{33} = -\frac{\Delta t}{2\Delta x} \left(\frac{\partial \Gamma_{p,i-1/2}^{k,m+1}}{\partial n_{p,i-1}} \right) \quad C_{34} = 0$$

$$C_{41} = -\frac{5\Delta t}{6\Delta x} \left(\frac{\partial \Gamma_{\varepsilon,i-1/2}^{k,m+1}}{\partial \varphi_{i-1}} \right) \quad C_{42} = 0 \quad C_{43} = 0 \quad C_{44} = -\frac{5\Delta t}{6\Delta x} \left(\frac{\partial \Gamma_{\varepsilon,i-1/2}^{k,m+1}}{\partial (n_e u_e)_{i-1}} \right)$$

Values for b_i vector (b₄ not yet validated):

$$b_1 = \left(\frac{(\varphi_{i+1}^{k,m+1}) - 2(\varphi_i^{k,m+1}) + (\varphi_{i-1}^{k,m+1})}{(\Delta x)^2} \right) + \frac{q \cdot n0}{\varepsilon_0} (n_{p,i}^{k,m+1} - n_{e,i}^{k,m+1})$$

$$b_2 = \frac{\Delta t}{2\Delta x} \left((\Gamma_{e,i+1/2}^{k,m+1} - \Gamma_{e,i-1/2}^{k,m+1}) + (\Gamma_{e,i+1/2}^{k,m} - \Gamma_{e,i-1/2}^{k,m}) \right) -$$

$$\Delta t \left(v \left[\frac{(n_e u_e)_i^{k,m+1}}{n_{e,i}^{k,m+1}} \right] \right) n_{e,i}^{k,m+1} + n_{e,i}^{k,m+1} - n_{e,i}^{k,m}$$

$$b_3 = \frac{\Delta t}{2\Delta x} \left((\Gamma_{p,i+1/2}^{k,m+1} - \Gamma_{p,i-1/2}^{k,m+1}) + (\Gamma_{p,i+1/2}^{k,m} - \Gamma_{p,i-1/2}^{k,m}) \right) -$$

$$\Delta t \left(v \left[\frac{(n_e u_e)_i^{k,m+1}}{n_{e,i}^{k,m+1}} \right] \right) n_{p,i}^{k,m+1} + n_{p,i}^{k,m+1} - n_{p,i}^{k,m}$$

$$\begin{aligned}
b_4 &= (n_e u_e)_i^{k,m+1} - (n_e u_e)_i^{k,m} + \frac{5\Delta t}{6\Delta x} \left((\Gamma_{\varepsilon,i+1/2}^{k,m+1} - \Gamma_{\varepsilon,i-1/2}^{k,m+1}) - (\Gamma_{\varepsilon,i+1/2}^{k,m} - \Gamma_{\varepsilon,i-1/2}^{k,m}) \right) \\
&\quad - \frac{\Delta t}{4\Delta x} (\Gamma_{\varepsilon,i+1/2}^{k,m+1} - \Gamma_{\varepsilon,i-1/2}^{k,m+1}) \cdot (\phi_{i+1}^{k,m+1} - \phi_{i-1}^{k,m+1}) + \Delta t \cdot k_L \left[\frac{(n_e u_e)_i^{k,m+1}}{n_{e,i}^{k,m+1}} \right] \cdot n_{e,i}^{k,m+1} N
\end{aligned}$$

Appendix C. Transport/Rate Coefficients Fit

BOLSIG fit for the electron mobility (17):

$$\begin{aligned}
 (u_e \leq 0.543) &\rightarrow \mu_e p = 1.6e6 \\
 (0.543 < u_e \leq 1.6) &\rightarrow \mu_e p = -6.08301e5 \cdot u_e + 1.81062e6 \\
 (1.6 < u_e \leq 5.207) &\rightarrow \mu_e p = (-23.87736 \cdot u_e + 922.45227)^2 \\
 (5.207 < u_e \leq 7.087) &\rightarrow \mu_e p = (3.487968 \cdot u_e + 785.6738)^2 \\
 (7.087 < u_e \leq 10.08) &\rightarrow \mu_e p = (8.084379 \cdot u_e + 752.824841)^2 \\
 (10.08 < u_e \leq 21.85) &\rightarrow \mu_e p = 16794.7345 \cdot u_e + 5.3014e5 \\
 (21.85 < u_e \leq 53.68) &\rightarrow \mu_e p = 6252.12852 \cdot u_e + 7.6784e5 \\
 (53.68 < u_e) &\rightarrow \mu_e p = 1.45550e5 \cdot \ln(u_e) + 5.17329e5 \\
 \mu_e [SI] &= \frac{\mu_e p}{(10^4)p}
 \end{aligned}$$

BOLSIG fit for the electron diffusion (17):

$$\begin{aligned}
 (u_e \leq 6.75) &\rightarrow D_e p = 3.65887e5 \cdot u_e + 4.63643e5 \\
 (6.75 < u_e \leq 10.0) &\rightarrow D_e p = -4.86929e5 \cdot u_e - 3.5917e5 \\
 (10.0 < u_e \leq 25.0) &\rightarrow D_e p = 8380.8 \cdot (u_e)^2 + 4.50769e5 \cdot u_e - 8.55212e5 \\
 (25.0 < u_e \leq 100.0) &\rightarrow D_e p = 8.70618e5 \cdot u_e - 7.0e6 \\
 (100.0 < u_e \leq 200.0) &\rightarrow D_e p = 9.48006e5 \cdot u_e - 1.4e7 \\
 (200.0 < u_e \leq 385.0) &\rightarrow D_e p = 1.05e6 \cdot u_e - 3.0e7 \\
 (385.0 < u_e) &\rightarrow D_e p = 3.7e8 \\
 D_e [SI] &= \frac{D_e p}{(10^4)p}
 \end{aligned}$$

Gas Parameter File (SIGLO-RF) fit for the ion mobility (18):

$$\begin{aligned}
 (E/P < 10.0) &\rightarrow \mu_p p = -73.967 \cdot (E/P) + 8725.8 \\
 (E/P \geq 10.0) &\rightarrow \mu_p p = \exp(9.9) \cdot (E/P)^{-0.35226} \\
 \mu_p [SI] &= \frac{\mu_p p}{(10^4)p}
 \end{aligned}$$

BOLSIG fit for ionization rate (17):

$$\begin{aligned}
(u_e \leq 2.53) &\rightarrow v_i / p = 0.0 \\
(2.53 < u_e \leq 2.88) &\rightarrow v_i / p = 0.02 \\
(2.88 < u_e \leq 3.26) &\rightarrow v_i / p = 0.33 \\
(3.26 < u_e \leq 7.34) &\rightarrow v_i / p = 1.3e3 \cdot \exp(2.3112 \cdot u_e) \\
(7.34 < u_e \leq 8.45) &\rightarrow v_i / p = 3.47826e - 11 \cdot (u_e)^{17.326} \\
(8.45 < u_e \leq 9.47) &\rightarrow v_i / p = 8.57143e - 6 \cdot (u_e)^{11.525} \\
(9.47 < u_e \leq 12.4) &\rightarrow v_i / p = 0.2138 \cdot (u_e)^{7.0431} \\
(12.4 < u_e \leq 49.92) &\rightarrow v_i / p = 7.1e6 \cdot u_e - 7.7e7 \\
(49.92 < u_e) &\rightarrow v_i / p = 2.4e8 \cdot \ln(u_e) - 6.6e8 \\
v_i[SI] &= (v_i / p)p
\end{aligned}$$

BOLSIG fit for ionization rate (17):

$$\begin{aligned}
(u_e = 0) &\rightarrow k_L = 0.0 \\
(u_e \leq 5.21) &\rightarrow k_L = 2.0e - 12 \cdot (u_e)^2 + 1.3e - 11 \cdot u_e - 2.6e - 12 \\
(5.21 < u_e \leq 7.09) &\rightarrow k_L = 4.37e - 11 \cdot (u_e)^3 - 7.25e - 10 \cdot (u_e)^2 + 4.05e - 9 \cdot u_e - 7.46e - 9 \\
(7.09 < u_e \leq 9.8) &\rightarrow k_L = 8.0e - 10 \cdot (u_e)^2 + 1.1255e - 8 \cdot u_e - 6.6e - 8 \\
(9.8 < u_e) &\rightarrow k_L = 4.23e - 7 \\
(8.45 < u_e \leq 9.47) &\rightarrow v_i / p = 8.57143e - 6 \cdot (u_e)^{11.525} \\
(9.47 < u_e \leq 12.4) &\rightarrow v_i / p = 0.2138 \cdot (u_e)^{7.0431} \\
(12.4 < u_e \leq 49.92) &\rightarrow v_i / p = 7.1e6 \cdot u_e - 7.7e7 \\
(49.92 < u_e) &\rightarrow v_i / p = 2.4e8 \cdot \ln(u_e) - 6.6e8 \\
k_L[SI] &= \frac{k_L}{10^6}
\end{aligned}$$

Bibliography

1. Corke, Thomas C. Eric J. Jumper, Martiqua L. Post, Dmitriy Orlov and Thomas E McLaughlin. "Application of Weakly-Ionized Plasmas as Wing Flow-Control Devices", AIAA Press, Washington DC, 2003, paper 2002-0350.
2. Post, Martiqua L. and Thomas C. Corke, "Separation Control on High Angle of Attack Airfoil Using Plasma Actuators", *41st Aerospace Sciences Meeting and Exhibit*, Reno, NV, 6-9 January 2003, paper 2003-1024.
3. Roth, J. Reece. "Aerodynamic flow acceleration using paraelectric and peristaltic electrohydrodynamic effects of a One Atmosphere Uniform Glow Discharge Plasma." *Physics of Plasmas* 10:2117-2126 (May 2003).
4. Nasser, Essam. *Fundamentals of Gaseous Ionization and Plasma Electronics*. New York: Wiley-Interscience, 1971.
5. Von Engel, A. *Ionized Gases: Second Edition*. Oxford: Oxford University Press, 1965.
6. Eliasson, Baldur. "Modeling and Applications of Silent Discharge Plasmas," *IEEE Transactions on Plasma Science*, 19:309-323 (April 1991).
7. Boeuf, J.P. "Plasma display panels: physics, recent developments and key issues." *Journal of Physics D: Applied Physics*, 36:R53-R79 (2003).
8. Hilbun, William M., "Workshop on Modeling Dielectric Barrier Discharges For Plasma Actuators." PowerPoint presentation, 13 May 2004.
9. Raizer, Yu P. *Gas Discharge Physics*. Berlin: Springer-Verlag, 1991.
10. Hagelaar, G.J.M. *Modeling of Microdischarges for Display Technology*. Technische Universiteit Eindhoven, Eindhoven, The Netherlands, November 2000.
11. Howatson, A.M.. *An Introduction to Gas Discharges: Second Edition*, Oxford: Pergamon Press, 1976.
12. Font, Gabriel I. "Boundary Layer Control with Atmospheric Plasma Discharges." *40th AIAA/ASME/SAE/ASEE Joint Propulsion Conference and Exhibit*, Ft. Lauderdale, FL, 11-14 July 2004, paper AIAA 2004-3574.
13. Enloe, C.L., Thomas E. McLaughlin, Robert D. VanDyken and K.D. Kachner. "Mechanisms and Responses of a Single Dielectric Barrier Plasma." *41st*

Aerospace Sciences Meeting and Exhibit, Reno, NV, 6-9 January 2003, paper AIAA 2003-1021.

14. Boeuf, J.P. and L. C. Pitchford. "Two-dimensional model of a capacitively coupled rf discharge and comparisons with experiments in the Gaseous Electronics Conference reference reactor." *Physical Review E*, 51:1376-1384 (February 1995).
15. Boeuf, J.P., A. Fiala and L.C. Pitchford. "Two-dimensional, hybrid model of low-pressure glow discharges." *Physical Review E*, 49:5607-5622 (June 1994).
16. Hilbun, William M. and Benjamin J. Case. "Preliminary Development of a Computational Model of a Dielectric Barrier Discharge." *49th AIAA Aerospace Sciences Meeting and Exhibit*, Reno, NV, 10-13 January 2005, paper AIAA 2005-1176.
17. *BOLSIG*. Version 1.05, PC Windows 95 & NT. Computer software. Kinema Software & CPAT, Monument, CO and Toulouse, France, December 1996.
18. *SIGLO-RF*. Version 1.0, PC. Computer software. Kinema Software, Monument, CO, March 1995.
19. Morgan, W.L., J.P. Boeuf and L.C. Pitchford. *BOLSIG: Users Guide*. Monument, CO: Kinema Software, Toulouse, France: CPAT, March 1995.
20. Kinema Research Associates. *SIGLO-RF: The RF Discharge Modeling Software-PC Version 1 User's Guide*. Monument, CO: Kinema Software, March 1995.
21. Cravens, Thomas E., Alexander J. Dessler, John T. Houghton, Michael J. Rycroft. *Physics of Solar System Plasmas*. New York: Cambridge University Press, 1997.
22. Dendy, R.O. *Plasma Dynamics*. New York: Oxford University Press, 1990.
23. Ward, A.L. "Calculations of Cathode-Fall Characteristics." *Journal of Applied Physics*, 33:2789-2794 (September 1962).
24. Shang, J.S., Sergey T. Surzhikov and Domenic D'Ambrosio. "Plasma Modeling Program Delivery Order", Contract No. F33615-03-3307, Task 1, Final Technical Report.
25. Boeuf, J.P., C. Punset, S. Cany. "Addressing and sustaining in alternating current coplanar plasma display panels." *Journal of Applied Physics*, 86:124-133 (1 July 1999).

26. Gummel, H.K. and D.L. Scharfetter. "Large-Signal Analysis of a Silicon Read Diode Oscillator." *IEEE Transactions on Electron Devices*, 16:64-77 (January 1969).
27. Hilbun, William. "MN Approach to Modeling Plasma Actuators." UF/GERC (Shalimar, FL), 13 May 2004.
28. Braun, Dieter, Valentin Gibalov and Gerhard Pietsch. "Two-dimensional modeling of the dielectric barrier discharge in air." *Plasma Sources Science Technology*, 1:166-174 (1992).
29. Sjöberg, M., Yu. V. Serdyuk, S.M. Gubanski, M.Å.S. Leijon. "Experimental study and numerical modeling of a dielectric barrier discharge in hybrid air-dielectric insulation." *Journal of Electrostatics*, 59:87-113 (2003).
30. Press, William H., Saul A. Teukolsky, William T. Vetterling and Brian P. Flannery. *Numerical Recipes in C: The Art of Scientific Computing*. New York: Cambridge University Press, 1995.
31. Fletcher, C.A.J.. *Computational Techniques for Fluid Dynamics, Volume 1* (2nd Edition). Heidelberg, Germany: Springer-Verlag, 1991.
32. Hoffman, Klaus A. and Steve T. Chiang. *Computational Fluid Dynamics for Engineers: Volume I*. Wichita, KS: Engineering Education System, 1993.
33. Daniels, Allen. "Tridiagonal Solver Method." Java Code. n. pag. <http://www3.interscience.wiley.com:8100/legacy/college/epperson/0471316474/java/chapter2/TridiagonalSolver.java.pdf>. 13 December 2004.
34. Chapra, Steven C. and Raymond P. Canale. *Numerical Methods for Engineers* (3rd Edition). Boston, MA: McGraw Hill, 1988.
35. McGrath, Joseph. "Solve a System of Non-Linear Equations." n. pag. <http://www.usedmath.com/SeveralEquations.htm>. 1 April 2005.
36. Poggie, J. and D.V. Gaitonde. "Electrode Boundary Conditions in Magnetogasdynamic Flow Control." *40th Aerospace Sciences Meeting and Exhibit*, 14-17 January 2002, Reno, NV, paper AIAA 2002-0199.
37. Lieberman, Michael A. and Allan J. Lichtenberg. *Principles of Plasma Discharges and Materials Processing*. New York: John Wiley & Sons, Inc., 1994.

38. Boeuf, J. P. "Numerical model of rf glow discharges." *Physical Review A*, 36:2782-2792 (September 1987).
39. Brauer, I., C. Punset, H.-G. Purwins and J.P. Boeuf. "Simulations of self-organized filaments in a dielectric barrier glow discharge plasma." *Journal of Applied Physics*, 85,:7569-7572 (June 1999).
40. Hammond, E.P., K. Mahesh and P. Moin. "A Numerical Method to Simulate Radio-Frequency Plasma Discharges." *Journal of Computational Physics*, 176, 2002.

REPORT DOCUMENTATION PAGE				Form Approved OMB No. 074-0188	
<p>The public reporting burden for this collection of information is estimated to average 1 hour per response, including the time for reviewing instructions, searching existing data sources, gathering and maintaining the data needed, and completing and reviewing the collection of information. Send comments regarding this burden estimate or any other aspect of the collection of information, including suggestions for reducing this burden to Department of Defense, Washington Headquarters Services, Directorate for Information Operations and Reports (0704-0188), 1215 Jefferson Davis Highway, Suite 1204, Arlington, VA 22202-4302. Respondents should be aware that notwithstanding any other provision of law, no person shall be subject to a penalty for failing to comply with a collection of information if it does not display a currently valid OMB control number.</p> <p>PLEASE DO NOT RETURN YOUR FORM TO THE ABOVE ADDRESS.</p>					
1. REPORT DATE (DD-MM-YYYY) 06-06-2005		2. REPORT TYPE Master's Thesis		3. DATES COVERED (From – To) Sep 2004 – Jun 2005	
4. TITLE AND SUBTITLE Computational Model of One-Dimensional Dielectric Barrier Discharges				5a. CONTRACT NUMBER	
				5b. GRANT NUMBER	
				5c. PROGRAM ELEMENT NUMBER	
6. AUTHOR(S) Marchand, Krista G., Captain, USAF				5d. PROJECT NUMBER	
				5e. TASK NUMBER	
				5f. WORK UNIT NUMBER	
7. PERFORMING ORGANIZATION NAMES(S) AND ADDRESS(S) Air Force Institute of Technology Graduate School of Engineering and Management (AFIT/EN) 2950 Hobson Way WPAFB OH 45433-7765				8. PERFORMING ORGANIZATION REPORT NUMBER AFIT/GAP/ENP/05-05	
9. SPONSORING/MONITORING AGENCY NAME(S) AND ADDRESS(ES) N/A				10. SPONSOR/MONITOR'S ACRONYM(S)	
				11. SPONSOR/MONITOR'S REPORT NUMBER(S)	
12. DISTRIBUTION/AVAILABILITY STATEMENT APPROVED FOR PUBLIC RELEASE; DISTRIBUTION UNLIMITED.					
13. SUPPLEMENTARY NOTES					
14. ABSTRACT A one-dimensional fluid model of a surface-type dielectric barrier discharge is created using He as the background gas. This simple model, which only considers ionizing collisions and recombination in the electropositive gas, creates an important framework for future studies into the origin of experimentally observed flow-control effects of the DBD. The two methods employed in this study include the semi-implicit sequential algorithm and the fully implicit simultaneous algorithm. The first involves consecutive solutions to Poisson's, the electron continuity, ion continuity and electron energy equations. This method combines a successive over-relaxation algorithm as a Poisson solver with the Thomas algorithm tridiagonal routine to solve each of the continuity equations. The second algorithm solves an $Ax=b$ system of linearized equations simultaneously and implicitly. The coefficient matrix for the simultaneous method is constructed using a Crank-Nicholson scheme for additional stability combined with the Newton-Raphson approach to address the non-linearity and to solve the system of equations. Various boundary conditions, flux representations and voltage schemes are modeled. Test cases include modeling a transient sheath, ambipolar decay and a radio-frequency discharge. Results are compared to validated computational solutions and/or analytic results when obtainable. Finally, the semi-implicit method is used to model a DBD streamer.					
15. SUBJECT TERMS Dielectric Barrier Discharge, DBD, Flow-control, Numerical Fluid Approach, Computational Plasma Dynamics, Streamer Formation					
16. SECURITY CLASSIFICATION OF:			17. LIMITATION OF ABSTRACT UU	18. NUMBER OF PAGES 111	19a. NAME OF RESPONSIBLE PERSON William F. Baiely (ENP)
a. REPORT U	b. ABSTRACT U	c. THIS PAGE U			19b. TELEPHONE NUMBER (Include area code) (937) 255-3636, ext 4501; e-mail: William.Bailey@afit.edu